Effects of strongly eddying oceans on multidecadal climate variability in the Community Earth System Model

André Jüling[1], Anna von der Heydt[1], and Henk A. Dijkstra[1]

[1]Institute for Marine and Atmospheric research Utrecht (IMAU), Utrecht University, Netherlands

Correspondence: André Jüling (a.juling@uu.nl)

Abstract. Climate variability on multidecadal time scales appears to be organized in pronounced patterns with clear expressions in sea surface temperature, such as the Atlantic Multidecadal Variability and the Pacific Decadal Oscillation. These patterns are now well studied both in observations and global climate models and are important in the attribution of climate change. Results from CMIP5 models have indicated large biases in these patterns with consequences for ocean heat storage variability and eventually the global mean surface temperature. In this paper, we use two multi-century Community Earth System Model simulations at coarse ($1°$$1°$) and fine ($0.1°$$0.1°$) ocean model horizontal grid spacing to study the effects of the representation of mesoscale ocean flows on major patterns of multidecadal variability. We find that resolving mesoscale ocean flows both improves the characteristics of the modes of variability with respect to observations and increases the amplitude of the heat content variability in the individual ocean basins. ~~The effect on the~~ In the strongly eddying model, multidecadal variability increases compared to sub-decadal variability. This shift of spectral power is seen in sea surface temperature indices, basin-scale surface heat fluxes, as well as the global mean surface temperature~~is relatively minor~~.

Keywords. Multidecadal Climate Variability

Mesoscale ocean flows

Ocean Heat Content

Global Mean Surface Temperature

1 Introduction

The ocean plays a key role in the climate system's heat budget, absorbing some 93% of the additional heat retained due to anthropogenic greenhouse gases (Stocker et al., 2013). Although the instrumental record of sea surface temperature (SST) is only about one and a half centuries, the observations indicate the existence of spatially correlated patterns of variability on multidecadal time scales, also referred to as (statistical) modes of variability (Deser et al., 2010). These modes are thought to be part of the internal variability of the climate system and they affect the oceanic heat content by altering heat fluxes and consequently the global energy budget (Trenberth and Shea, 2006; Dijkstra, 2013; Zhang and Wang, 2013; Frajka-Williams et al., 2017).

Disentangling these modes of internal variability from forced changes is hence important for detection and attribution studies of

25 anthropogenic climate change ~~(Zhang et al., 2019a)~~(Hegerl and Zwiers, 2011; Bindoff et al., 2013; Deser et al., 2020). Indeed, these SST patterns have played a major role in the search for the origin of the most recent global mean surface temperature trend slowdown (Kosaka and Xie, 2013; England et al., 2014). They may also reflect a memory component of the climate system, which can provide enhanced skill in long-term climate predictions (Zhang et al., 2019a). On a broader perspective, societies are impacted significantly by these SST patterns through associated changes in ~~ecosystem productivity (Mantua et al., 1997) and~~

30 temperature extremes (e.g. Ruprich-Robert et al. (2018), droughts (e.g. McCabe and Palecki (2006); Delworth et al. (2015)), hurricanes (e.g. Zhang and Delworth (2006)), precipitation patterns (Sutton and Hodson, 2005~~.~~, and ecosystem productivity (Mantua et al., 1997). (Zhang et al., 2019b) reviews the climate impacts of the Atlantic Multidecadal Variability.

To determine patterns of SST variability, scalar indices measuring average SST anomalies over one or more regions are often regressed on the global SST field (Deser et al., 2010). Both the North Atlantic and North Pacific are known for their

35 low frequency SST variability and associated pattern. The Atlantic mode, indicated by the average North Atlantic SST, was ~~first~~ described by Kushnir (1994) and named the Atlantic Multidecadal Oscillation by ~~Kushnir (1994)~~Kerr (2000), but in the absence of a single spectral peak, we use the more modern naming convention of Atlantic Multidecadal Variability (AMV). Low frequency Pacific variability was revealed through ~~principle~~ principal component analysis of North Pacific SSTs (Pacific Decadal Oscillation; Mantua et al. (1997)) and of the global SSTs (Interdecadal Pacific Oscillation; Power et al. (1999)).

40 The Pacific Decadal Oscillation (PDO) is thought to arise as a combination of low frequency tropical variability and local air-sea interaction (Newman et al., 2016). In the Southern Ocean, SST observations are relatively sparse prior to satellite observations, but signatures of multidecadal variability are found, for example, in the Antarctic sea ice extent (Simpkins et al., 2013). Southern Ocean variability is assessed here through an SST index in the Atlantic sector of the Southern Ocean ~~where~~ (Le Bars et al., 2016). This Southern Ocean Mode (SOM) is a mode of multidecadal variability and is presumably the result of

45 eddy-mean flow interaction ~~can result in multidecadal variability (Le Bars et al., 2016; Hogg and Blundell, 2006; Jüling et al., 2018)~~ (Hogg and Blundell, 2006; Jüling et al., 2018).

The global mean surface temperature (GMST) signal comprises to a large extent the global mean SST signal. The SST is coupled to the surface heat flux (SHF) albeit in a complex manner. Generally, higher SSTs lead to a loss of heat from the oceans, but there is substantial geographic and seasonal variability depending on atmospheric conditions such as wind speed and cloud

50 presence (Park et al., 2005). There are qualitative differences in this air-sea interaction feedback between non-eddying and strongly eddying coupled climate models where the latter match the observed behaviour much better (Small et al., 2020). The ocean heat content (OHC) can influence the SST and is changed by both the SHF and heat divergence (Roberts et al., 2017). Multidecadal OHC changes are related to the three modes discusses here. In the mid-latitude North Atlantic, sub-decadal atmospheric variability drives the SHF, but low frequency changes in SST drive the SHF on time scales longer than 10 years

55 (Gulev et al., 2013). The observed Atlantic OHC changes are strongly modulated by the AMV (Häkkinen et al., 2015). The PDO SST pattern is replicated in the upper 300 m vertically integrated OHC (Kumar and Wen, 2016). The SOM was first described as a mode of OHC variability with an associated SHF pattern in the Southern Ocean Atlantic sector (Le Bars et al., 2016).

The importance of internal ocean variability in low-frequency climate variations has become more clear in recent years by comparing ocean model results forced by either climatological or observed atmospheric forcing (Penduff et al., 2014). Multidecadal SST variability can arise from a range of processes (Dijkstra, 2013). Energy can be shifted to lower frequencies by integration of high-frequency variability in one component by a slower component of a system, such as the coupled atmosphere-ocean system (Hasselmann, 1976). It can also arise from internal variability in the atmosphere which is imprinted through heat fluxes on the upper ocean (Eden and Jung, 2001). Internal multidecadal variability in the ocean can arise through specific instabilities, such as the thermal Rossby wave mechanism (Te Raa and Dijkstra, 2002). Results of idealized models have indicated that patterns of internal multidecadal SST variability may arise through noise excited (non)-normal modes (Frankcombe et al., 2009; Weijer and van Sebille, 2014; Dijkstra, 2016) or due to a collective interaction of such modes (Berloff et al., 2007b; Hogg and Blundell, 2006). Such collective interactions can change the vertical heat transport, affecting the stratification which in turn influences the response of the mixed layer to heat fluxes and/or wind stress (Manucharyan et al., 2017) or impact deep convection at multidecadal timescales (Dufour et al., 2017). Mesoscale eddies can also interact with the mean flow, for example through rectification, which can lead to changes in momentum and vorticity input by wind stress (Hogg and Blundell, 2006; Berloff et al., 2007a). Last, nonlinear advection of kinetic energy in the western boundary current separation region can lead to an inverse temporal cascade in which spectral energy is shifted from high to low frequencies (Martin et al., 2019).

Models participating in phase 5 of the Coupled Model Intercomparison Project (CMIP5; Taylor et al. (2012)) generally underestimate multidecadal climate variability (Cheung et al., 2017; Mann et al., 2020). The amplitudes of Pacific and Atlantic multidecadal variability, as measured by the AMV and PDO indices, are significantly lower than in observations. Further, the regression patterns partially mismatch those in observations, in particular in the Pacific and the western boundary current regions (Kajtar et al., 2019). Hence, CMIP5 models may miss crucial physical processes causing the patterns of multidecadal variability. The resolution of many, if not all, CMIP5 models is too coarse to capture all relevant internal variability. In at least one ocean model, multidecadal variability appears in a high resolution (strongly eddying) setup but is absent at a lower resolution (non-eddying) version (Le Bars et al., 2016).

Decreasing the horizontal ocean grid spacing from ~~$1°$~~ $1°$ in CMIP5 style GCMs to ~~$0.1°$~~ $0.1°$ enables new physics with the explicit representation of mesoscale phenomena (Tulloch et al., 2011; Hallberg, 2013). Mesoscale variability arises due to barotropic and baroclinic instability and affects the ocean state in myriad ways (McWilliams, 2008), for example by changing the advection of tracers (in particular affecting the heat and salinity budgets), affecting (re-)stratification (Couvelard et al., 2015; Dufour et al., 2017), and by modifying the mean flow through rectification. Mesoscale eddies also form an integral part of the turbulent energy cascade connecting ~~large scale~~ large-scale potential and kinetic energy input to small-scale dissipation. Currents, such as narrow western boundary currents, are also much better represented in high resolution simulations as are inter-ocean exchanges of water masses, most notably Agulhas rings (Biastoch et al., 2008).

In most CMIP5 model simulations, mesoscale eddy effects are parametrized with the isopycnal slope mixing parametrization of Gent and McWilliams (1990) (GM). While GM captures many effects of eddies on the circulation, it stabilizes the ocean state and suppresses low frequency variability (Hallberg and Gnanadesikan, 2006; Viebahn et al., 2018). Furthermore, GM does not capture rectification effects of the eddies on the mean flow. In idealized non-eddying ocean models, modes of multidecadal

variability exist that depend critically on the prescribed eddy diffusivity (Huck et al., 2014). Increasing the resolution to allow mesoscale eddies, Huck et al. (2014) find that the multidecadal variability persists despite changes in the mean circulation, suggesting that the eddy parametrization may suppress such low-frequency variability if tuned incorrectly. In a comparative study with a suite of coupled GFDL models at different resolutions, Griffies et al. (2015) find a stronger upward heat transport by the mesoscale eddies which counteracts the general downward heat transport by the mean currents. This enhanced vertical heat transport leads to larger heat fluxes and faster adjustment to forcing (Delworth et al., 2012).

With the availability of multi-century simulations of global climate models with strongly eddying ocean components (Kirtman et al., 2012; van Westen and Dijkstra, 2017), with a typical horizontal grid spacing of 10 km or less, it is timely to investigate how the mesoscale ocean flows affect the patterns of multidecadal variability. It is exactly what we do here in this paper, using simulations with the Community Earth System Model. The paper is organized as follows: section 2 describes the simulations and the methods of analysis, section 3 presents the results, and section 4 discusses and summarizes the results and their implications.

2 Model Simulations and Data Analysis

We analyze results from two multi-century present-day control simulations with the Community Earth System Model version 1.0.4 (CESM, Hurrell et al. (2013)), carried out at the Academic Computing Center in Amsterdam (SURFsara), see e.g., van Westen and Dijkstra (2017). Both control simulations use constant year 2000 atmospheric greenhouse gas concentrations forcing, notably ~~[CO₂] = 367 ppm and [CH₄] = 1760 ppb~~ $[CO_2]$ = 367 ppm and $[CH_4]$ = 1760 ppb. The CESM components are CAM5 (Community Atmosphere Model), POP2 (Parallel Ocean Program), CICE (sea ice model), and CLM (Community Land Model) which are coupled by the CESM1 coupler. The high resolution ~~(HIGH) simulation employs a 0.1°~~ simulation ('HR-CESM') employs a 0.1°ocean horizontal grid spacing on a tripolar grid, while the low resolution (~~LOW~~'LR-CESM') simulation has a ~~1°~~1°ocean horizontal grid spacing with a displaced dipolar grid. The effect of subgrid-scale processes on tracer and momentum transport is captured with a biharmonic diffusion operator in ~~the HIGH simulation~~ HR-CESM and the GM parameterization in ~~the LOW simulation~~ LR-CESM (Gent and McWilliams, 1990). The ~~HIGH~~ HR-CESM simulation was initialized from a simulation of several decades provided by the National Center for Atmospheric Research, while the ~~LOW~~ LR-CESM simulation was initialized from a ~~decally~~ decadally averaged ocean state at year 1000 of a CESM 1.1.2 simulation performed with the same resolution. CESM 1.1.2 and CESM 1.0.4 exhibit only minor differences in their ocean state with CESM 1.0.4 having slightly higher SSTs (not shown). Table 1 summarizes the important simulation characteristics.

Table 1. Overview of the two CESM simulations with characteristics and names of their ocean and atmosphere grids.

name	ocean grid	atmosphere grid	years analyzed
~~HIGH~~HR-CESM	~~0.1°~~0.1°tripole, 42 levels to 6000 m (`tx0.1v2`)	~~0.47° × 0.63°~~0.47°×0.63°(`f05`)	51-300
~~LOW~~LR-CESM	~~1°~~1°dipole, 60 levels to 5500 m (`gx1v6`)	~~0.9° × 1.25°~~0.9°×1.25°(`f09`)	11-260

From earlier simulations with the same model components (CCSM3.5: Kirtman et al. (2012) and CESM1: Small et al. (2014)), it is known that the climatology of the higher resolution simulation improves compared to the lower resolution simulation in many aspects. The overall SST biases reduce due to a better representation of boundary currents, ocean upwelling, and air-sea interactions (Small et al., 2014). Some biases remain, though, such as too warm high latitude SSTs which result in low sea ice extent and sea ice volume biases in the high resolution simulation (Kirtman et al., 2012).
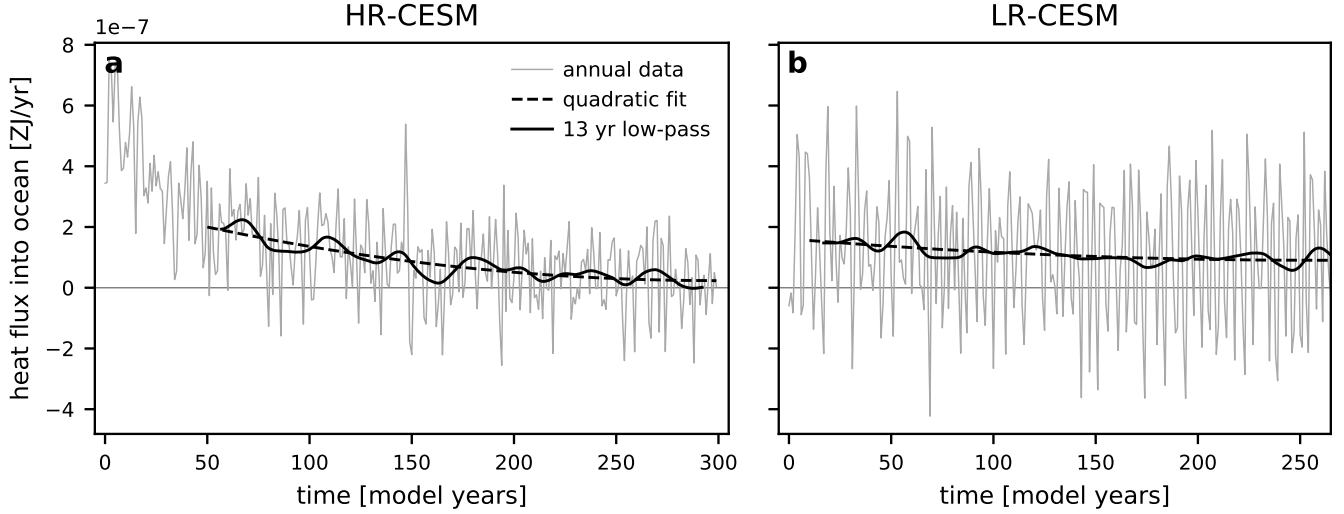
Figure 1. The globally averaged surface heat flux into the ocean of the ~~HIGH~~ HR- (a) and ~~LOW~~ LR-CESM (b) simulations including the annual time series (thin), the quadratic fit to the 250 analyzed model years (dashed), and the 13 year low-pass filtered version (solid). For the low-pass filtered time series, 7 years are removed at each end to avoid filter edge effects.

Figure 1 shows the global mean surface heat flux into the ocean indicating the equilibration of the simulations. The ~~HIGH~~ HR-CESM simulation equilibrates significantly faster than the ~~LOW~~ LR-CESM simulation. The GFDL CM2 climate models show a similarly decreased drift in their higher resolution setups which is due to ~~an~~ enhanced upward heat transport by the explicitly resolved eddies (Delworth et al., 2012; Griffies et al., 2015). In our CESM simulations, all basins are initiated too cool and hence the temperature increases at all depths, except for the deep Pacific and some layers at intermediate depths in the Indian Ocean which cool (not shown). On interannual time scales, the Pacific surface heat fluxes vary strongest in comparison with those in the other basins. In particular, in ~~the LOW simulation~~ LR-CESM a too strong El Niño-Southern Oscillation (ENSO) signal dominates the global interannual surface heat flux signal (Fig. 1b; Wieners et al. (2019)).

The results in Fig. 1 indicate that a trend must be removed despite the constant forcing as the model simulations are still adjusting towards their statistical equilibrium. We remove a quadratic trend at each grid point of the relevant model output. This approach allows for different proximities to the statistical equilibrium and different time scales of adjustment at each grid cell. A further choice in the analysis is the selection of model years which are used in the analysis. ~~Of the HIGH simulation we~~ We ignore the first 50 HR-CESM spinup years as strong adjustment is evident in the global mean SST approximately until

year 40. As mentioned, the ~~LOW~~ LR-CESM simulation is initialized at year 1000 of a CESM 1.1.2 simulation with the same forcing and grid that maintains a ~~near constant~~ near-constant surface heat flux of 2.2 ZJ yr^{-1} concurrent to the ~~LOW~~ LR-CESM simulation. We choose to discard the first 10 years of data to avoid fast adjustment processes and analyze years 11-260 (cf. Table 1). Monthly data is ~~de-seasonalized~~ deseasonalized by removing the mean ~~annual cycle, i. e. the mean monthly difference to the annual mean.~~ seasonal cycle.

To compare the SST model results with observations, we use the HadISST sea surface temperature dataset from 1870-2018 which is provided on a ~~1° × 1°~~ 1°×1° grid (Rayner et al., 2003). The observational dataset must be detrended with an appropriate estimate of the historical forced signal to allow for a fair comparison with the results of the model simulations, which are obtained under constant forcing. A simple linear detrending is unable to remove the non-linear historical forcing signal (Steinman et al., 2015). When an ensemble of model simulations is available, the forced signal can be approximated as the ensemble mean assuming that the internal variability of the individual ensemble members is uncorrelated. One can use either the mean of a single model ensemble (such as that of the Max-Planck Institute Grand Ensemble (Maher et al., 2019) or the CESM Large Ensemble (Kay et al., 2015)) or a multi-model ensemble (multi-model mean: MMM; such as that of the CMIP5 ensemble). The MMM is generally superior to the single model ensemble mean in the historical period (Frankcombe et al., 2018), so we use CMIP5 ensemble results. The forced signal can furthermore be estimated as a single time series (single factor detrending; used for example by Steinman et al. (2015)) or as a linear combination of different forcing signals (multi-factor detrending as described below).

For the HadISST dataset, we choose to separate the natural and anthropogenic forcing signals which was found to be superior to single-factor detrending (Frankcombe et al., 2018). We use the CMIP5 MMM forced with observed aerosol and greenhouse gas concentrations until 2005 and those from the RCP8.5 scenario ~~afterwards~~ afterward until 2018 (like ~~,~~ e.g. Kajtar et al. (2019)). The natural forcing is assumed to equal the CMIP5 MMM of the historical (natural forcing only) simulations. The anthropogenic contribution (MMM_{ant}) due to greenhouse gases and aerosols is calculated as the difference between the fully forced MMM (MMM_{all}) and the MMM with only natural forcing (MMM_{nat}), i.e.,

$$MMM_{ant} = MMM_{all} - MMM_{nat} \tag{1}$$

At each grid point, scaled versions of these two time series are subtracted from the historical reconstructed SST, such that the detrended SST is

$$SST_{detr}(x,y,t) = SST(x,y,t) - \alpha_1(x,y)MMM_{nat}(t) - \alpha_2(x,y)MMM_{ant}(t) - \alpha_3(x,y) \tag{2}$$

where the coefficients α_i at each location are determined through multiple linear regression. Stolpe et al. (2017) show for the AMV index and the index of Pacific multidecadal variability by Henley et al. (2015) (which does not equal the PDO index, but shares characteristics) that the various detrending methods result in similar behavior.

From the deseasonalized and detrended model and observational SST fields, we determine area averages and principle components as indices of modes of multidecadal variability. The AMV index is calculated here over the domain [0°N,60°N]×[80°W,0°E], very similar to that in Stolpe et al. (2017) who use the zonal extent [75°W,5°W]. The PDO is captured by the first principal

component of the Pacific SSTs north of 20°N as originally proposed by Mantua et al. (1997). The Southern Ocean Mode (SOM) index, proposed by Le Bars et al. (2016) as a signature of the multidecadal variability in the Atlantic sector of the Southern Ocean, is computed over the region [50°S,35°S]×[50°W,0°E]. The index regions are outlined in the respective regression maps of Fig. 3. The indices are defined as the 13 year, second-order Butterworth low-pass filtered monthly time series with the first and last 7 years removed to avoid filter edge effects.

To assess the spatial expression of the modes of multidecadal variability, we use regression plots (Deser et al., 2010). The plotted regression values R are defined as the covariance of the SST field and the normalized index $X(t)$, where $X = $ AMV, PDO, or SOM, according to

$$R(x,y) = \frac{\text{cov}(\text{SST}(x,y,t), X(t))}{\text{std}(X(t))}, \tag{3}$$

such that R has units of temperature. The significance against a no-correlation null hypothesis is tested with a two-tailed Student's t-test. Because the time series are autocorrelated and filtered, the effective number of data points n' is lower than the original sample size n and can be estimated as the maximum of the reduced sample size due to filtering and due to autocorrelation (Trenberth, 1984):

$$n' = n \times \max\left(f\Delta t, \frac{1 - r_{1,X}r_{1,Y}}{1 + r_{1,X}r_{1,Y}}\right), \tag{4}$$

where $r_{1,X}$ ($r_{1,Y}$) is the lag-1 autocorrelation of time series X (Y), f the filtering frequency, and Δt the time step.

We analyze time series in the spectral domain with multi-taper spectra (Ghil et al., 2002). This estimator of spectral density is superior to the classic periodogram in that it reduces spectral leakage and is statistically robust, i.e. the estimated noise reduces with more data points. However, as a trade-off the effective spectral resolution is reduced which becomes problematic at periodicities near the length of the time series. We therefore limit our analysis to periodicities below 50 years when focussing on model-observation comparisons but extend the range to 100 year periods for comparisons between the simulations. We use a bandwidth parameter of 2 and the number of tapers is 3. To test significance against a red noise null hypothesis (Hasselmann, 1976), we generate 10,000 Monte-Carlo ~~first order~~ first-order autoregressive (AR(1)) processes. The autocorrelation coefficient and noise amplitude are estimated with the maximum likelihood estimator via Kalman filtering from the deseasonalized and detrended but unfiltered monthly time series ~~Durbin and Koopman (2012)~~(Durbin and Koopman, 2012).

Beyond analyzing spectral peaks above red noise null hypotheses, we quantify aspects of the spectra by calculating the mean over the multidecadal and interannual time scales as well as fitting a multidecadal spectral slope (Dee et al., 2017; Parsons et al., 2017). We define multidecal variability ('MV') and interannual to sub-decadal variability ('IV') with periods between 10 and 50 years and 2 and 10 years, respectively. To avoid overfitting to higher frequencies when calculating the means and slope, we first bin the spectral estimates in the logarithmic frequency space. We use 8 log-equidistant bins for both the MV and IV intervals. The MV mean spectral power serves as a direct comparison between spectra, while the MV/IV ratio speaks to the relative strength of variability between these two frequency windows. The spectral slope indicates the relative strength of low frequency spectral power to high frequency decadal power within the MV window. A negative spectral slope is called red with enhanced spectral power at low frequencies, a positive slope blue with less power at low frequencies, and a near-zero slope white with approximately equal power at all frequencies.

We define the zonally and vertically integrated OHC anomaly, OHC_v, as

$$\mathrm{OHC}_v(y,t) = c_p \int \int \rho\theta(x,y,z,t)\ \mathrm{d}x\,\mathrm{d}z\ , \tag{5}$$

where θ is the potential temperature, ρ the density, and c_p = 3996 J kg^{-1} K^{-1} the seawater heat capacity used in the CESM. The horizontally integrated OHC anomaly $\mathrm{OHC}_h(z,t)$ is

$$\mathrm{OHC}_h(z,t) = c_p \int \int \rho\theta(x,y,z,t)\ \mathrm{d}x\,\mathrm{d}y, \tag{6}$$

210

The HR-CESM temperature data has been interpolated to a 0.4°rectangular grid and the OHC calculations were performed on that grid. This interpolation introduces very little error and enables the calculation of zonal integrals. The LR-CESM OHC is calculated on the original displaced dipole grid and zonal integrals are performed along the grid x-direction (so not along parallels in the high northern latitudes).

3 Results

215

The results are divided into four subsections: the first describes the variability in SST by means of the chosen indices, the second focuses on the surface heat fluxes (SHF), the third explores the spatial structure of multidecadal variability of the Ocean Heat Content (OHC), and the fourth shows the consequences for the Global Mean Surface Temperature (GMST).

3.1 Sea Surface Temperature

220 ~~From the deseasonalized and detrended model and observational SST fields, we determine area averages and principle components as indices of modes of multidecadal variability. The AMV index is calculated here over the domain $[0°N, 60°N] \times [80°W, 0°E]$, very similar to that in Stolpe et al. (2017) who use the zonal extent $[75°W, 5°W]$. The PDO is captured by the first principal component of the Pacific SSTs north of as originally proposed by Mantua et al. (1997). The Southern Ocean Mode (SOM) index, proposed by Le Bars et al. (2016) as a signature of the multidecadal variability in the Atlantic sector of the Southern~~

225 ~~Ocean, is computed over the region $[50°S, 35°S] \times [50°W, 0°E]$. The index regions are outlined in the respective regression maps of Fig. 3. The indices are defined as the 13 year Butterworth low-pass filtered monthly time series with the first and last 7 years removed to avoid filter edge effects.~~ Figure 2 shows the AMV, PDO, and SOM indices which all display variability at multidecadal time scales (Fig. 2a-c). The AMV and SOM indices (in units of Kelvin) exhibit a smaller amplitude in the simulations than in the historical data (Fig. 2d). ~~Both~~ The standard deviations are calculated via the stationary bootstrapping method

230 to avoid biases due to the different time series lengths (Politis and Romano, 1994). Both AMV and SOM amplitudes are higher in ~~the HIGH simulation than in the LOW simulation. Larger PDO amplitudes after lowpass filtering of the underlying monthly~~ ~~,~~HR-CESM than in LR-CESM. The unfiltered monthly PDO time series has unit standard deviation ~~time series indicate larger spectral power~~ by construction. The PDO amplitude after low-pass filtering (Fig. (Fig. 2d) is larger in the observations than in the models. This indicates that a larger proportion of spectral power is at frequencies below the filter cutoff frequency of

235 13 years.
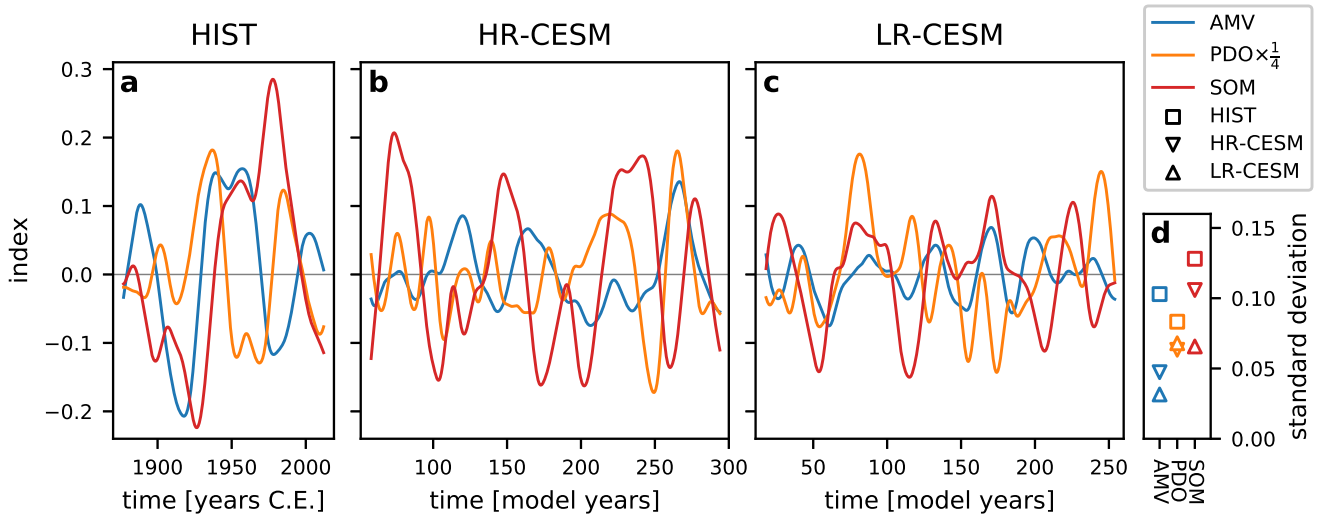
Figure 2. The three 13 year low-pass filtered indices of multidecadal variability for the two-factor detrended HadISST data (a) and the quadratically detrended ~~HIGH~~ HR- (b) and ~~LOW~~ LR-CESM (c) simulations. Atlantic Multidecadal Variability (blue) and Southern Ocean Mode (red) indices are in units of Kelvin. The monthly time series of the Pacific Decadal Oscillation index (orange) is dimensionless ~~with unit standard deviation is also low-pass filtered~~ and has been ~~divided here by 4~~ scaled for a comparable amplitude to the ~~other~~ AMV and SOM indices~~(orange)~~. At each end of the time series, 7 years are removed to avoid filter edge effects. Panel (d) shows the standard deviation of the low-pass filtered time series derived via stationary bootstrapping.

Figure 3 shows the regression patterns of the detrended SST on the AMV, PDO, and SOM indices for the detrended historical data (HIST) and the two simulations (~~HIGH and LOW~~HR- and LR-CESM). For the AMV index, the regression pattern of the detrended historical SST data shows a horse-shoe shape with significant positive regression values throughout the North Atlantic, with a maximum in the subpolar gyre and a secondary maximum in the subtropical gyre. The regression patterns
240 of both ~~HIGH and LOW~~ HR- and LR-CESM simulations show a comparable pattern to the historical data, albeit with lower regression values. Like the observations, ~~the HIGH simulation~~ HR-CESM exhibits the strongest regression values in the subpolar gyre, while ~~the LOW simulation~~ LR-CESM shows more pronounced regression values in the subtropical gyre. ~~The LOW simulation~~ LR-CESM exhibits significant negative correlations inside the horseshoe pattern that are not present in the historical observations or ~~the HIGH simulation~~HR-CESM. In the historical data and the ~~HIGH~~ HR-CESM simulation regression values
245 are smaller in magnitude outside of the North Atlantic, but the ~~LOW~~ LR-CESM simulation's tropical Pacific exhibits positive correlation values exceeding those in the North Atlantic. Both simulations show a significant ENSO/PDO-like regression pattern in the Pacific and dipole structure in the Indian Ocean, whereas the historical data shows only largely non-significant positive correlations in the tropical Pacific and ~~a~~ positive correlations throughout the northern Indian Ocean. Overall, the areas of significant correlations are larger in ~~the LOW simulation~~ LR-CESM than in both the ~~HIGH~~ HR-CESM simulation and
250 the historical data. This suggests possible teleconnections between the Indian and Pacific basins and the Atlantic basin at
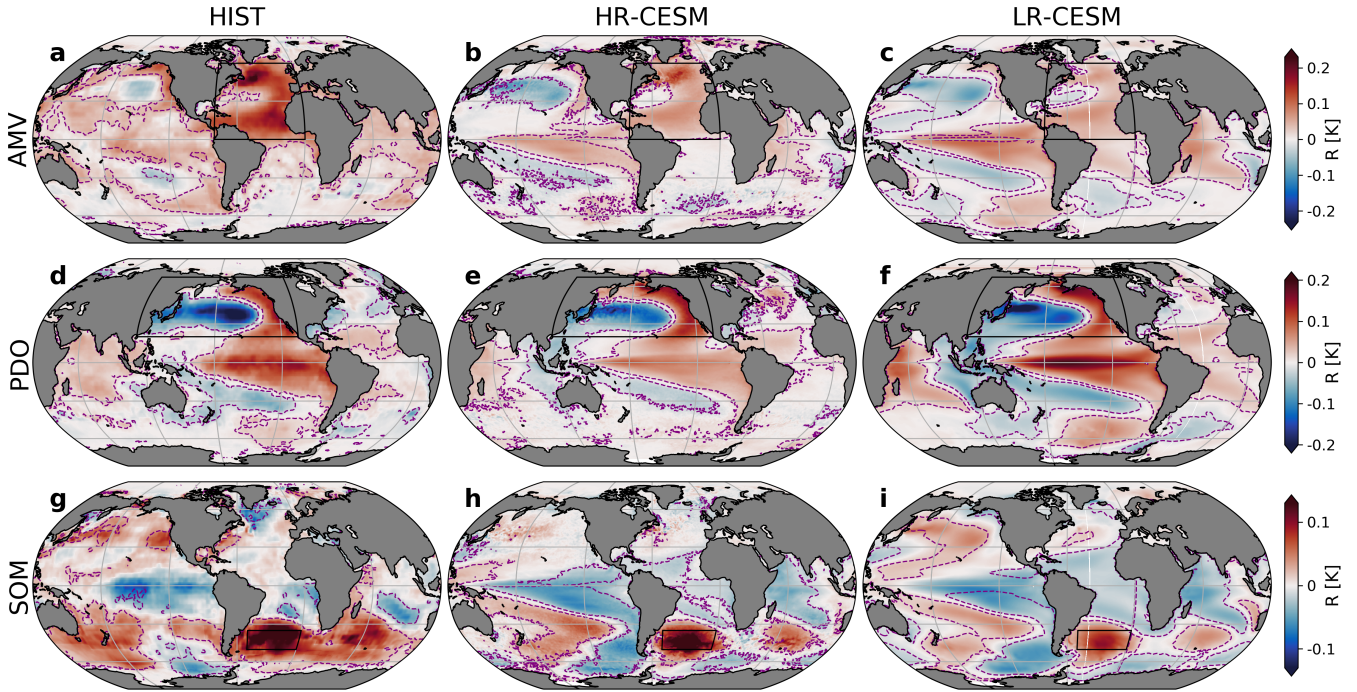
Figure 3. Regression maps (values of R(x, y) as in eqn. 3 in Kelvin) of the detrended SST fields onto the AMV (a-c), PDO (d-f), and SOM (g-i) indices for the 149 year detrended HadISST historical dataset (left) and the 250 year data sets of ~~HIGH~~ HR- (center) and ~~LOW~~ LR-CESM (right) simulations. Purple dashed lines demarcate the areas of significant correlations at the 98% level. Black boxes outline the index areas. Parallels and meridians are drawn every ~~30°~~ 30° and ~~60°~~ 60°, respectively. Note the different colorbar ranges.

multidecadal time scales especially in ~~the LOW simulation~~LR-CESM, but such correlations are not significant in observations ~~(Steinman et al., 2015).~~ of North Pacific and North Atlantic SSTs (Steinman et al., 2015). The insignificance of the correlations in the observations may be a sign of absent teleconnections, but could also be due to a host of other reasons. these include, for example, sparse early observations, the signal being removed by the (necessarily imperfect) detrending approach, or a non-stationary nature of teleconnections, as suggested for tropical modes variability by Cai et al. (2019).

The PDO regression pattern is characterized by negative values in the Kuroshio extension and positive values in an enclosing horseshoe pattern to the East. In the observations, the minimum is located east of the dateline and significant positive values exist in the Eastern tropical Pacific. Weaker negative (positive) regression values ~~exists~~ exist in the southwest Pacific (the Bellingshausen Sea). The simulations show largely similar patterns, although the minima in the Kuroshio extension area are shifted west of the dateline, especially so in ~~the LOW simulation~~LR-CESM. The historical data shows uniformly positive correlations in the Indian Ocean where both simulations display a dipole pattern which is more pronounced in ~~the LOW simulation~~LR-CESM. All PDO patterns exhibit positive values in the tropical Pacific, but the ~~regression values of the LOW~~

~~simulation~~ LR-CESM regression values are closer to those of the historical data. In ~~the LOW simulation~~ LR-CESM a large area of significant correlations in the tropical Atlantic exists that is absent in both the observations and ~~HIGH simulation~~HR-CESM.

The SOM index regression pattern shows a coherent pattern spanning much of the Southern Ocean at significant levels in the historical data with maximum values in the SOM region and a secondary maximum north of the Kerguelen Plateau in the West Indian Ocean sector of the Southern Ocean. Both simulations exhibit these two positive value areas and whereas the ~~HIGH~~ HR-CESM simulation's correlation values are closer to those of the historical SST data, both feature a more azonal pattern with negative values in the Eastern Weddell Gyre. All patterns exhibit negative regression values in the tropical Pacific, but only the simulations feature this structure at significant levels and then as part of a larger South Pacific horseshoe shape pattern that extends south to the Bellingshausen Sea; there, slightly negative values occur in the observations as well. ~~The LOW~~ The LR-CESM simulation's area of significant correlations extends further into the Northern Hemisphere, especially in the Pacific.

Figure 4 shows the spectral power of the unfiltered monthly ~~index time series of~~ AMV, PDO, and SOM index time series. Again, the historical indices cover 149 years while the simulated ones cover 250 years, resulting in different spectral resolutions. ~~To allow a comparison between the results, also the period of variability of the historical data has been extended to~~ We show the spectra up to a period of 50~~years, although the higher period results are less reliable than in the models,~~ years, but note that the spectral estimate of the historical indices is less reliable at low frequencies because of the ~~difference in data series length . In the detrended observations, significant (99%) spectral power for all three indices occurs at large periodicities above 40 years. The PDO signal also extends beyond the red noise (95%) at periods of about 20 years.~~ shorter time series length compared to the model estimates. Most previously published spectral ~~analysis~~ analyses of the North Atlantic observed temperatures find significant periodicities around 50-70 years, but ~~they overwhelmingly~~ almost all remove a linear trend only which distorts the signal (Steinman et al., 2015). Longer proxy data records reveal significant multi-decadal variability around the North Atlantic from sources including Greenland ice cores (Chylek et al., 2011), tree rings (Gray et al., 2004), sediments (Knudsen et al., 2011), or a combination of proxies (Delworth and Mann, 2000; Wang et al., 2017). ~~In the HIGH simulation, significant spectral power~~ Palaeo reconstructions have also been performed of the PDO (D'Arrigo et al., 2001; MacDonald, 2005; Felis et al., 2010; O'Mara et al., 2019).

In the detrended observations, significant (99%) spectral power for all three indices occurs at periodicities above 40 years. The PDO signal also extends beyond the red noise (95%) at periods of about 20 years. In HR-CESM, significant spectral power peaks only exist at 40-50 years for the AMV index (>95%), around 13-15 and 20-25 years for the PDO index (>99%), ~~while the SOM index shows significant variability~~ and around 15 years (>95%) and above 40 years (>95%) ~~. The indices of the LOW simulation~~ for the SOM index. The LR-CESM indices exhibit no significant spectral power for either the AMV or SOM indices and the red noise null hypothesis cannot be rejected at 95% level, and only the PDO index has a significant spectral peak (95%) at 16 years. The quantitative measures of the spectra in the multidecadal variability (MV; 10-50 years) and interannual variability (IV; 2-10 years) bands include the MV spectral slope (purple), the mean MV spectral power, and the MV/IV mean power ratio. For all indices, the MV/IV ratio is larger in HR- than in LR-CESM and in the case of AMV and SOM closer to the historical indices. The MV mean power and MV/IV ratio of the AMV are much larger and the spectral slope is much redder in the detrended historical data than in the simulations. The PDO historical and HR-CESM MV slopes are red (negative) while
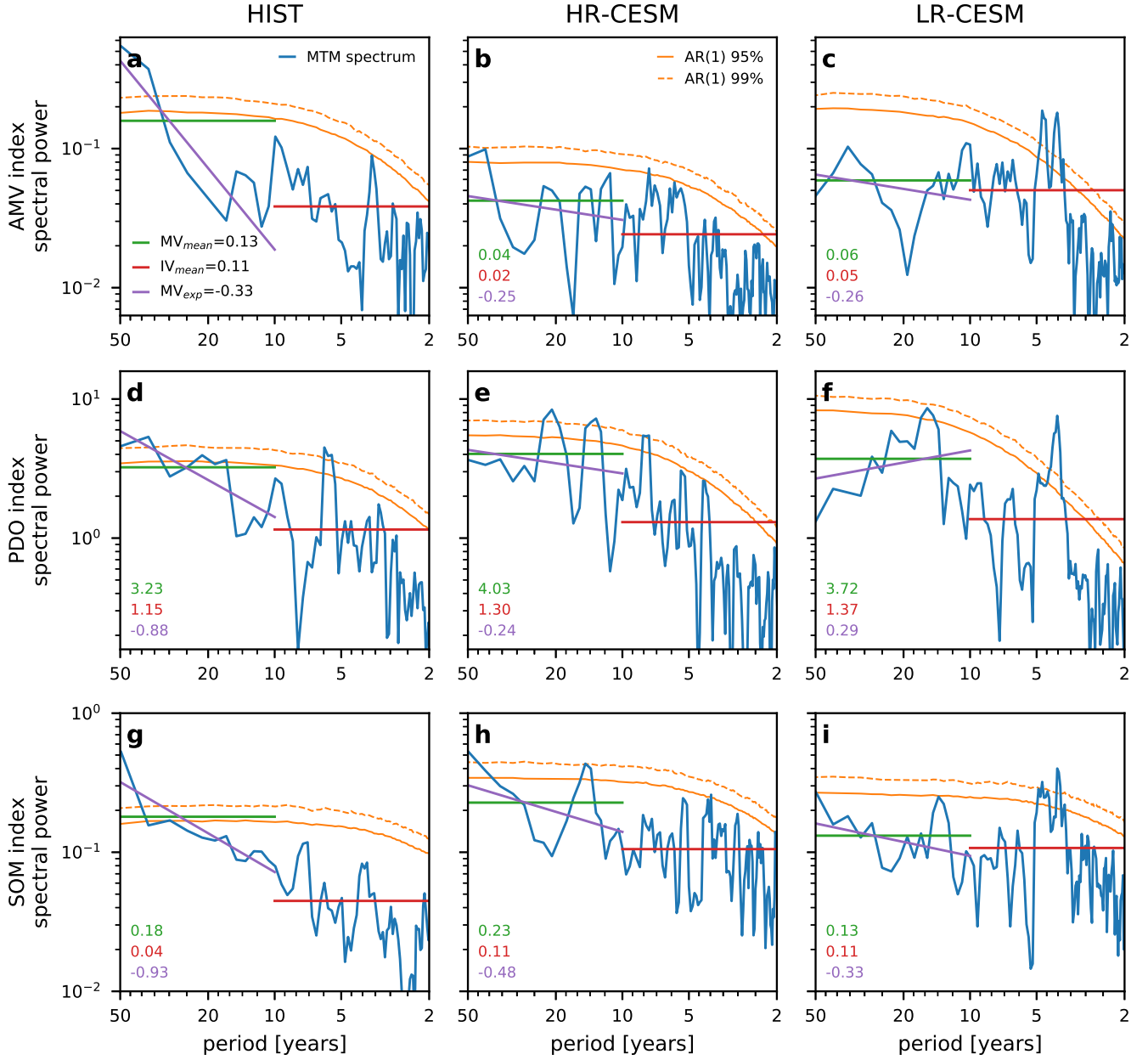
Figure 4. Multi-taper spectral estimates of the unfiltered monthly SST indices (blue) underlying the filtered time series of Fig. 2. Panels (a-c) show the AMV, (d-f) the PDO, and (g-i) the SOM index spectra for the two-factor detrended 149 year HadISST dataset (left) and the 250 year ~~HIGH~~ HR- and ~~LOW~~ LR-CESM simulations (center and right, respectively). The units of the spectral power are [K^2 yr] for the SST average AMV and SOM indices and [yr] for the dimensionless PDO index~~which is dimensionless as a principal component~~. As a null hypothesis, 10,000 AR(1) processes were simulated to estimate the 95% and 99% red noise confidence interval (solid and dashed orange lines). The horizontal green and red lines represent the mean spectral power in the multidecadal variability (MV; 10-50 years) and the interannual (IV; 2-10 years). The purple line is a linear fit to the spectral slope in the MV band. Numbers refer to the mean values (red/green) and the slope (purple).

it is blue (positive) in LR-CESM. The SOM MV slope of HR-CESM is redder than that of LR-CESM and thus closer to the slope of the historical SOM index.

3.2 Surface Heat Fluxes

Figure 5 shows the time series and spectra of the surface heat flux (SHF) into the global ocean ~~(black)~~ as well as into the major ocean basins~~(Atlantic: blue, Pacific: orange, Southern Ocean: red). We define the Southern Ocean as south of the parallel at Cape Agulhas at~~. The Global Ocean (black) includes all ocean basins and marginal seas, the Atlantic Ocean (blue) is bounded in the north by the Labrador Sea and extends to Iceland, ~~while the Pacific~~ the Pacific (orange) extends up to the Bering Strait~~(,~~ while our Southern Ocean (red) is located south of the parallel at Cape Agulhas at 34°S (inset map in Fig. 5b). For global as well as Atlantic and Pacific heat fluxes, the ~~LOW~~ LR-CESM spectra show enhanced power around 4 and 8 years which is due to a strong and regular ENSO in this simulation ~~.~~ (Fig. 5c/d). At multidecadal time scales ~~, the HIGH simulation clearly exhibits larger surface heat flux variability than~~ (10-50 years; MV in Fig. 5d), HR-CESM exhibits larger SHF variability than LR-CESM with the exception of the Atlantic. In particular, the ~~LOW simulation in particular in the Southern Ocean and, as a result, globally. The Atlanticand Pacific SHF spectral comparison is more subtle, as there are periods between 25-35 years where the LOW simulation shows higher variability than the HIGH simulation. However, the integrated Atlantic and Pacific multidecadal spectral poweris higher in the HIGH simulation compared to the LOW simulation. Remarkable is further that the Southern Ocean SHF spectrum is nearly white with similar power at all frequencies, while both the Atlantic and Pacific show decreasing power at lower frequencies~~Southern Ocean shows enhanced MV spectral power and at lower frequencies than the 50 year MV cutoff all basin and the global SHF exhibit larger spectral power. The MV/IV ratio is larger and the MV spectral slopes are redder globally and for all basins for HR- than for LR-CESM.

3.3 Ocean Heat Content

The basin-scale ocean heat content (OHC) changes are largely determined by surface heat fluxes while horizontal heat divergences play a minor role. The strong multidecadal surface heat flux variability motivates the investigation of the structure of OHC anomalies in this section. Long reconstructions of the OHC exist for the industrial period (1870-2015; Zanna et al. (2019)) and even the Common Era (15-2015; Gebbie and Huybers (2019)), but they lack the detail that we aim to investigate here so that we compare model data only.

~~The HIGH simulation temperature data has been interpolated to a 0.4° rectangular grid and the OHC calculations were performed on that grid. The OHC of the LOW simulation is calculated on the original displaced dipole grid and zonal integrals are performed along the grid x-direction (so not along parallels in the high northern latitudes). The~~ The first two columns of Figure 6 are Hovmöller diagrams of 13 year low-pass filtered zonally and vertically integrated OHC anomalies, ~~indicated by OHC_v, i.e. ,~~

$$OHC_v(y,t) = c_p \int \int \rho\theta(x,y,z,t) \, \mathrm{d}x \, \mathrm{d}z \, ,$$
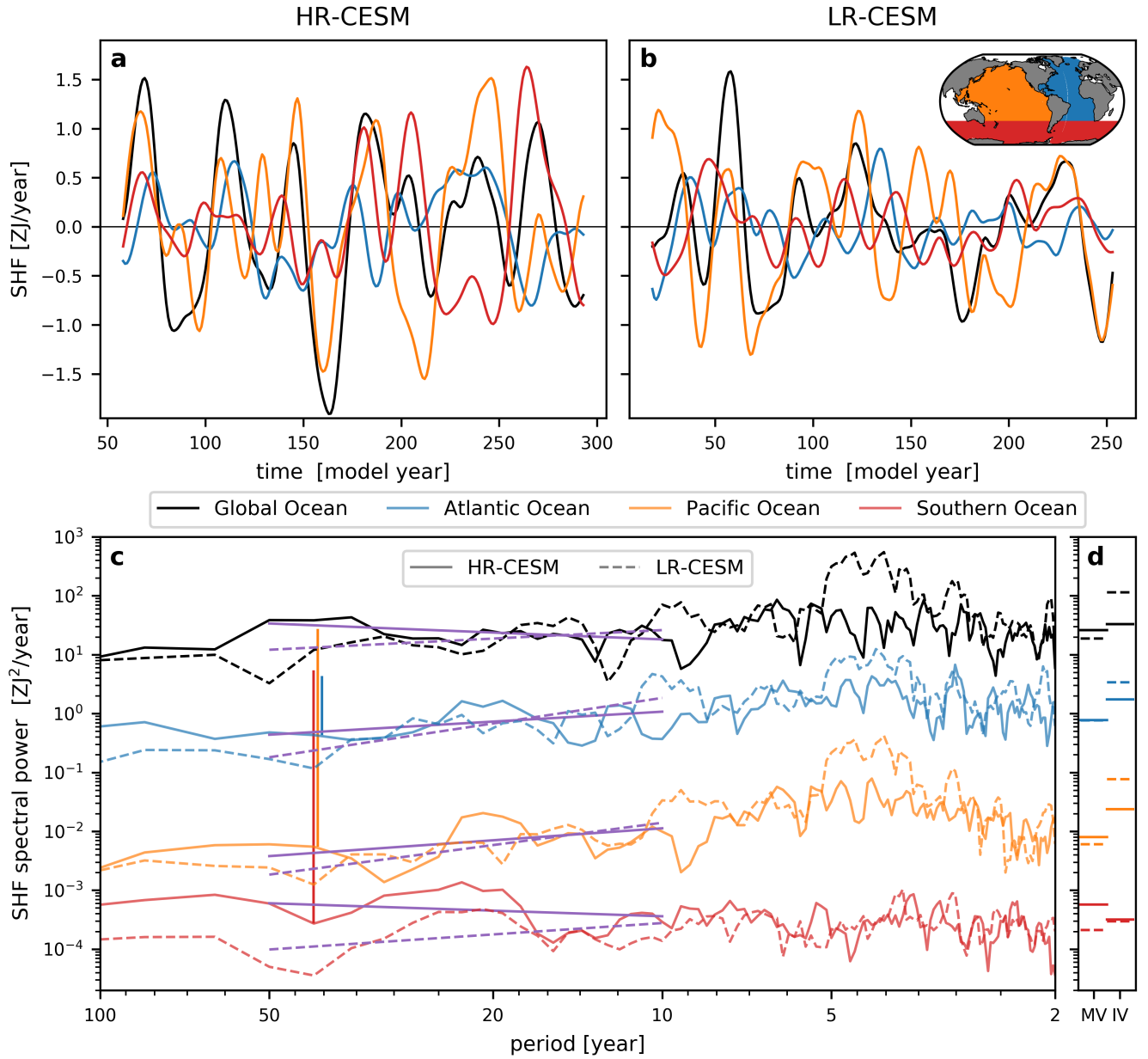
Figure 5. Time series for the 13 year low-pass filtered surface heat fluxes (SHF) into the global (black; equals thick solid line of Fig. 1), Atlantic (blue), Pacific (orange), and Southern (red) oceans for the HR- (a) ~~HIGH~~ and LR-CESM (b) ~~LOW~~ simulations. The inset global map defines the three major ocean basins. Panel (c) shows the multi-taper spectral estimates of the unfiltered, but ~~quadratially~~ quadratically detrended time series. The spectral slopes in the multidecadal variability band (MV; 10-50 years) are shown as purple lines. The spectral power means of the MV and interannual (IV; 2-10 years) bands are shown in panel (d). For visual clarity, the spectra were separated vertically by multiplying ~~the basin flux spectra~~ them by constant factors, these shifts are indicated by vertical lines.
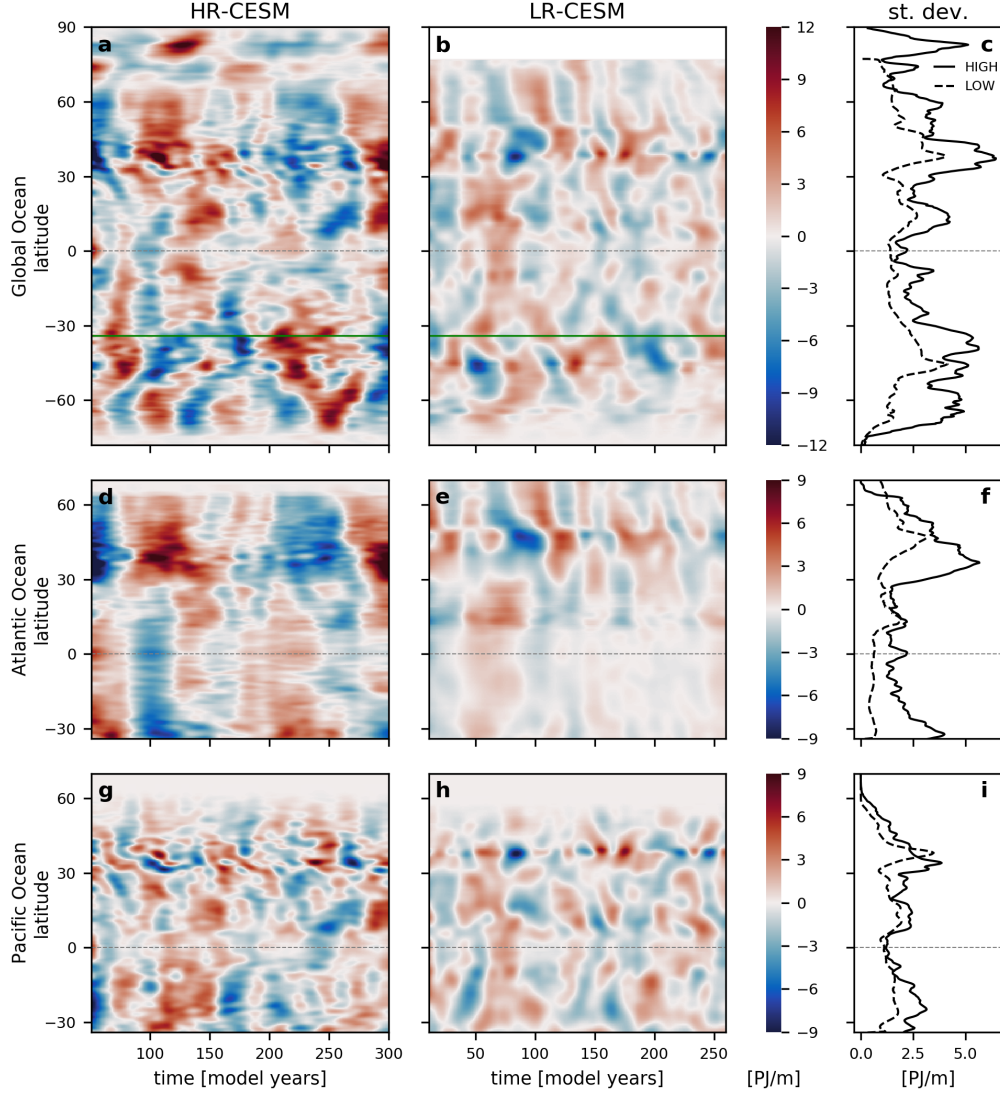
Figure 6. The 13 year low-pass filtered zonally and ~~depth integrated~~ depth-integrated OHC anomalies ($\text{OHC}_v(t, y)$ of Eq. (5)) as Hovmöller diagrams of the ~~HIGH~~ HR- (left) and ~~LOW~~ LR-CESM simulations (center), respectively. The top row shows the globally integrated OHC anomaly (which includes the Southern Ocean signal south of 34°S, demarcated with the green line in the first row), while the lower rows show the individual ocean basins. The equator is marked with a thin dashed line. The right column shows the standard deviation in time of the zonally and ~~depth integrated~~ depth-integrated OHC (solid: ~~HIGH~~HR-CESM, dashed: ~~LOW~~LR-CESM). The ~~LOW~~ LR-CESM latitudes values are averaged along the grid x-coordinate, such that north of 60°N they are not exactly representing the true latitudes. Note the different color scale ranges of each row with units of $\text{PJ/m} = 10^{15}\,\text{J/m}$.

~~where θ is the potential temperature, ρ the density, and $c_p = 3996\,\mathrm{J\,kg^{-1}\,K^{-1}}$ the sea water heat capacity used in the CESM.~~

330 $\mathrm{OHC}_v(y,t)$ (Eq. 5). The last column in Figure 6 shows the standard deviation of the 13 year low-pass filtered anomalies as a function of latitude. Almost everywhere the variability as measured by this standard deviation is higher in ~~HIGH compared to LOW~~HR-CESM than in LR-CESM. The first row shows the global signal which also captures the Southern Ocean signal south of 34°S (marked by the green line). ~~Here~~ In the HR-CESM Southern Ocean signs of the SOM ~~in the HIGH simulation~~ can be seen with north- and southward propagating anomalies; these are absent in ~~the LOW simulation~~LR-CESM. The Atlantic

335 behavior is qualitatively similar between ~~the HIGH and LOW simulations~~ HR- and LR-CESM with southward propagating anomalies between ~~and~~ 40°N and 10°N, although the anomaly amplitude is larger in ~~the HIGH simulation~~HR-CESM. Both simulations further show meridionally coherent anomalies south of 10°N in the Atlantic~~.~~, a pattern seen in observed OHC (Häkkinen et al., 2015). On the other hand, in the Pacific remarkable differences exist: only in the ~~HIGH simulation~~ HR-CESM OHC anomaly signals propagate equatorward around 30°N, imprinting on the global pattern as diagonal ridges

340 (compare subplots (g)&(a) with (h)&(b)). This is also visible to a lesser extent in the South Pacific just north of 30°S. In the equatorial Pacific, the unrealistically strong ~~ENSO signal of the LOW simulation~~ LR-CESM ENSO signal is filtered out by the 13 year low-pass filter. However, compared to the ~~HIGH~~ HR-CESM OHC_v, the difference is reduced between the tropical and extratropical low frequency spectral power as revealed by the standard deviations. The Atlantic and Pacific peaks at northern midlatitudes are shifted equatorward in ~~the HIGH simulation compared to the LOW simulation~~ HR-CESM compared to

345 LR-CESM due to a better representation of the western boundary current separation. ~~In the Indian Ocean, the HIGH simulation shows a less meridionally coherent pattern compared to the LOW simulation.~~

Figure 7 shows 13 year low-pass filtered Hovmöller diagrams of the horizontally integrated OHC anomalies, ~~given by~~

$$\mathrm{OHC}_h(z,t) = c_p \int \int \rho\theta(x,y,z,t)\ \mathrm{d}x\,\mathrm{d}y,$$

~~where the last column shows the temporal standard deviation at each depth.~~$\mathrm{OHC}_h(z,t)$ (Eq. 6). Globally and in the individual

350 ocean basins, ~~the HIGH simulation~~ HR-CESM exhibits stronger and deeper OHC variability than ~~the LOW simulation~~LR-CESM. The global OHC_h anomalies on multidecadal timescales are dominated by those in the upper 1200 m (Fig. 7c). The ~~HIGH~~ HR-CESM global multidecadal signal below the mixed layer is made up, in approximately equal parts, of the Atlantic, Pacific, and Southern Ocean components, as they exhibit similar magnitudes in their OHC_h standard deviations. In ~~the LOW simulation~~LR-CESM, the global anomalies are dominated by those in the Pacific. The Atlantic ~~HIGH~~ HR-CESM OHC_h

355 anomaly standard deviation shows a pronounced peak between 400 and 1500 m depth. In the Pacific, the variability is larger between 200 ~~m~~ and 1500 m in ~~the HIGH simulation~~HR-CESM. In the upper 1000 m, the anomalies propagate quickly downwards in the Atlantic but slower in the Pacific. At Pacific depths below 1000 m, a very slow downward propagation of anomalies is visible in ~~the HIGH simulation~~ HR-CESM that is absent in ~~the LOW simulation~~LR-CESM. The faster vertical propagation of heat anomaly signals in the Atlantic compared to the Pacific can be explained by the presence of the North Atlantic downward

360 branch of the meridional overturning circulation (Buckley and Marshall, 2016). In the Southern Ocean, large differences are evident: the ~~HIGH~~ HR-CESM multidecadal variability is much stronger and extends to the full depth as opposed to the ~~LOW~~
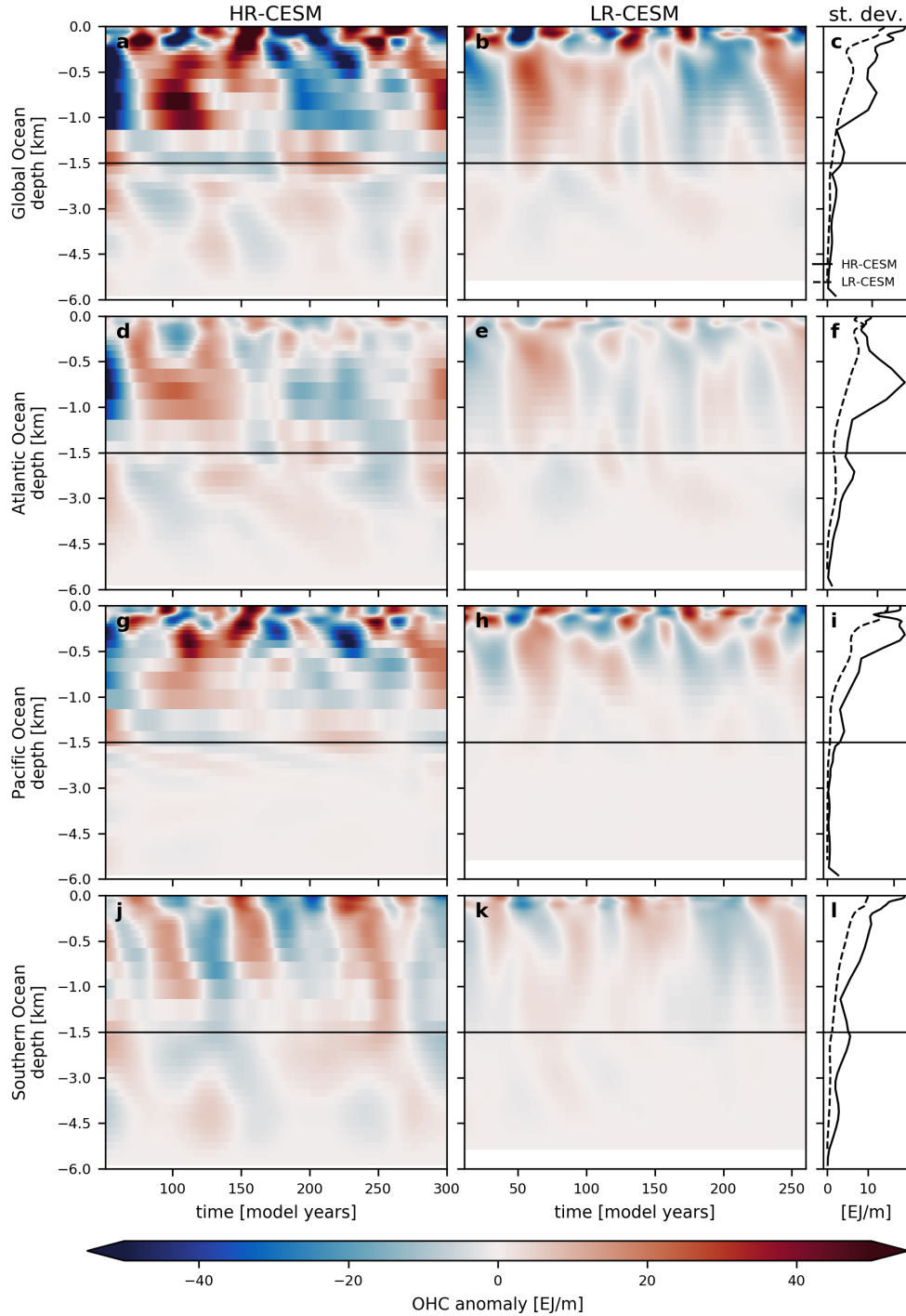
Figure 7. The 13 year low-pass filtered horizontally integrated OHC anomalies ($\mathrm{OHC}_h(t,y)$ of Eq. (6)) as Hovmöller diagrams of the ~~HIGH~~ HR- (left) and ~~LOW~~ LR-CESM (center) simulations, respectively. The different rows show the global, Atlantic, Pacific, and Southern Ocean integrals over time. Note the change of depth scale at 1500 m. The right column shows the standard deviation in time of horizontally integrated OHC (solid: ~~HIGH~~HR-CESM, dashed: ~~LOW~~LR-CESM), calculated similarly as in Fig. 6. Units are in $\mathrm{EJ/m} = 10^{18}\,\mathrm{J/m}$.

LR-CESM variability that is weaker at all depths, in correspondence with results in Le Bars et al. (2016). The SOM index (Fig. 2) correlates very well with Southern Ocean surface OHC$_h$ signal.

3.4 Global Mean Surface Temperature
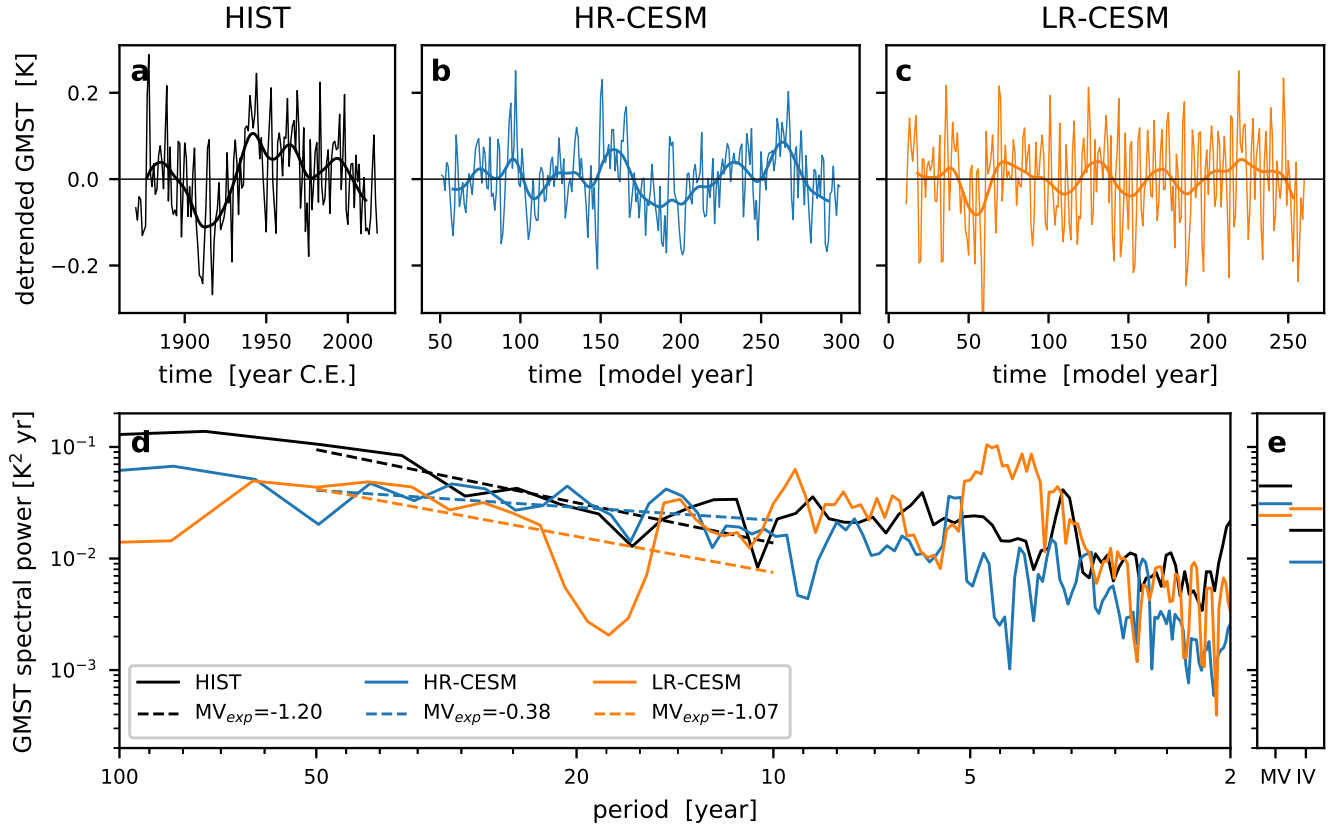
Figure 8. Time series ~~and multi-taper spectra~~ of the detrended annual global mean surface temperature . The historical GMST estimate is derived from (a-c; thin lines) and the ~~two-factor detrended~~ 13 year low-pass filtered time series ~~as discussed in section, while model (HR- and LR-CESMthick lines)~~. Multi-taper spectral estimates ~~are based on~~ from the ~~quadratically detrended~~ time series (d; solid lines) with the fitted spectral slopes between 50 and 10 years (dashed). Panel (e) shows the mean spectral power in the multidecadal (10-50 years) and interannual (2-10 years) bands.

365   The multidecadal global mean surface temperature (GMST) evolution is a consequence of the heat flux convergence in the atmosphere as energy is exchanged through the sea surface with the oceans and through the top of the atmosphere with outer space. Figure 8 shows the time series and spectral estimates of the GMST. At periods around 4 years, the too strong ~~ENSO of the LOW simulation~~ LR-CESM ENSO (as extensively ~~analysed~~ analyzed in Wieners et al. (2019)), leads to a larger interannual variability in the GMST time series and manifests ~~iteself~~ itself as a peak of the GMST spectral signal. At multidecadal time

370 scales (beyond periods of 13 years) the integrated spectral power in ~~the HIGH simulation~~ HR-CESM is higher than in ~~the LOW simulation~~LR-CESM, but for periodicities at 35-60 years the ~~LOW~~ LR-CESM GMST spectral power is higher than that of ~~the HIGH simulation~~HR-CESM. The spectral power of the two-factor detrended historical GMST data lies between both simulations at sub-decadal time scales, agrees well with both simulations at (inter-) decadal time scales, and exceeds both simulations at periods above 30 years. The MV mean spectral power of the HR-CESM is higher than from LR-CESM and

375 closer to the estimate from the detrended historical GMST. The MV/IV ratio of HR-CESM is similar to the historical estimate and both are much larger than for LR-CESM which even exhibits higher IV than MV power. The spectral slope, however, is less red for HR-CESM than for LR-CESM which is a result of the low LR-CESM spectral power between 16 and 24 years.

4   Summary and Discussion

We investigated the effect of ocean model resolution on multidecadal variability by contrasting two multi-century simu-

380 lations with the Community Earth System Model~~(CESM)~~, one with a non-eddying ocean typical of the CMIP5 models (~~LOW~~'LR-CESM') and one with a strongly eddying ocean (~~HIGH~~'HR-CESM'). The enhanced horizontal ocean model resolution allows for more detailed features of the circulation with many documented improvements, such as better representation of boundary currents, ~~reduced SST biases~~sea surface temperature (SST), air-sea ~~exchange~~exchanges, and internal variability of both high and low frequency relative to the ~~life times~~ lifetimes of mesoscale ocean eddies. In particular, we focused on three

385 modes of multidecadal SST variability: the Atlantic Multidecadal Variability (AMV), the Pacific Decadal Oscillation (PDO), and the Southern Ocean Mode (SOM). We find that these modes of multidecadal variability are more pronounced in the ~~HIGH~~ HR-CESM simulation than in the ~~LOW~~ LR-CESM simulation (Fig. 2) and compare more favourably to observations both in regression patterns (Fig. 3) and spectral properties (Fig. 4). At multidecadal time scales, stronger surface heat fluxes ~~(globally and in all major ocean basins)~~ are associated with this larger SST variability (Fig. 5). The integrated ocean heat content (OHC)

390 signal varies more strongly in ~~the HIGH simulation than in the LOW simulations~~ HR-CESM than in LR-CESM and anomalies extend to greater depths (Figs. 6, 7). However, while the integrated spectral power of the global mean surface temperature (GMST) at multidecadal ~~tie~~ time scales is larger in ~~the HIGH simulation than the LOW simulation~~HR- than in LR-CESM, there are frequencies at which the ~~LOW~~ LR-CESM GMST variability is larger (Fig. 8). For all analyzed quantities the MV/IV ratio is larger for HR-CESM than for LR-CESM and generally, the MV spectral slopes are redder and MV mean spectral

395 power higher in HR- compared to LR-CESM. As HR-CESM is consistently closer to observational estimates, we conclude that non-eddying coupled climate models potentially systematically underestimate low frequency variability. From the analyzed ~~LOW and HIGH CESM~~ HR- and LR-CESM simulations, we conclude that representing mesoscale eddies in the CESM leads to ~~an enhanced intensity of multidecadal variability in the ocean~~enhanced multidecadal variability.

In the Atlantic, an improvement in the simulation of the AMV pattern is evident in ~~the HIGH simulation compared to the~~

400 ~~LOW simulation.~~HR-CESM compared to LR-CESM (Fig. 3a-c). While the overall AMV pattern is similar in observations and model simulations, the HR-CESM subpolar maximum in the regression patterns ~~in the HIGH simulation~~ matches the detrended observations in contrast to ~~the subtropical maximum in the LOW resolution~~LR-CESM with its subtropical maximum.

Due to the specifics of our detrending approach, the historical regression pattern looks somewhat different from Deser et al. (2010), especially outside the North Atlantic. In particular, the pattern shows a statistically significant positive correlation in

405   the northwestern tropical Pacific that is not evident in the regression pattern of Deser et al. (2010). The AMV spectra also show that the ~~HIGH~~ HR-CESM simulation performs better compared with the historical SST data by showing significant power at multidecadal periodicities against the red noise null hypothesis, while the spectral estimate of the ~~LOW~~ LR-CESM AMV signal fails to reject this null hypothesis (Fig. 4). In CESM Large Ensemble control and historical simulations which uses CESM in the LR-CESM configuration, Kim et al. (2018) also find reduced MV spectral power in the AMV index compared

410   to historical estimates. While the magnitude of OHC variability is larger in ~~the HIGH simulation~~HR-CESM, the meridional and depth structures of the Atlantic OHC variability are similar between ~~the HIGH and LOW simulations~~ HR- and LR-CESM (Figs. 6~~7~~d-f 7d-f). This suggests that the AMOC effects on the OHC variability are captured with the coarse resolution in agreement with earlier studies (Delworth et al., 1993; Delworth and Mann, 2000) providing support for physical mechanisms of the AMV deduced from idealized models which are independent of mesoscale variability (Te Raa and Dijkstra, 2002).

415   Increasing the resolution can still improve the AMV relative to observations by reducing ocean mean state biases, in particular the representation of the Gulf Stream and of deep water formation.

We use the PDO index to capture Pacific low frequency variability and the resulting regression patterns are similar between observations and simulations ~~.~~(Fig. 3d-f). The spectral estimates of both the historical PDO and simulated ones extend beyond the 95% confidence interval interdecadal time scales around 20 year periodicity. ~~The LOW~~ The LR-CESM simulation exhibits

420   a ~~too~~ strong and regular ENSO signal (Wieners et al. (2019); visible e.g. in Fig. 5c) and the low frequency ~~tropical Pacific SHF spectral power~~ Pacific OHC_y standard deviation is relatively larger ~~than the extratropical spectral power compared to the HIGH simulation~~ in the tropics than the extratropics compared to HR-CESM (Fig. 5i). That the PDO partly comprises a low-frequency ENSO signal is visible in the strong tropical Pacific regression maximum ~~on the LOW simulation~~in LR-CESM. With the better representation of the western boundary currents in HR-CESM, in particular the Kuroshio, ~~in the HIGH simulation,~~

425   there are qualitative differences in the meridional structure of the Pacific OHC anomaly propagation: around 30°N, and to a lesser degree around 30°S, equatorward propagation is evident in ~~the HIGH simulation~~ HR-CESM while meridionally coherent anomalies appear in ~~the LOW simulation~~LR-CESM (Fig. 6).

The representation of the ~~Antarcic~~ Antarctic Circumpolar Current in the Southern Ocean changes dramatically between ~~the HIGH and LOW simulations~~ HR- and LR-CESM due to the presence of mesoscale eddies. The multidecadal SHF variabil-

430   ity is much enhanced in the strongly eddying ~~HIGH simulation~~ HR-CESM compared to the ~~LOW simulation.~~non-eddying LR-CESM (Fig. 5). Ocean heat anomalies also penetrate much deeper into the Southern Ocean, suggesting a crucial difference between explicitly simulated mesoscale eddies and their parametrization in advecting heat downward (Fig. 7). In ~~the HIGH simulation~~HR-CESM, the SOM is visible in the meridional structure with north- and southward moving anomalies, while anomalies simply converge on ~~in the LOW simulation~~ 45°S in LR-CESM (Fig. 6). The presence of the SOM is expected in

435   the ~~HIGH~~ HR-CESM simulation as it is thought to be caused by the interaction of mesoscale eddies and the mean flow (Hogg and Blundell, 2006; Le Bars et al., 2016; Jüling et al., 2018). However, the SOM regression patterns of the ~~HIGH and LOW~~ HR- and LR-CESM simulations are more similar to one another than to the observations with a more azonal, circumpolar

wavenumber-3 pattern and stronger correlations extending into the South Pacific ~~.~~ (Fig. 3g-i). However, the pattern in the HadISST dataset is likely to be biased due to the limited number of observations in this region, in particular prior to satellite
440 observations.

That strongly eddying climate models should simulate an increase in multidecadal variability relative to higher frequency variability is not immediately obvious as mesoscale eddies have relatively short lifetimes and small spatial scales. Multiple mechanisms through which mesoscale eddies can generate multidecadal variability have been alluded to in the introduction, such as eddy-mean flow interactions (Hogg and Blundell, 2006; Berloff et al., 2007a), the changes to the stratification introduc-
445 ing memory (Manucharyan et al., 2017) or the modification of conditions for convection (Dufour et al., 2017). Furthermore, only eddying models are capable of simulating observed high-frequency variability correctly (Penduff et al., 2011), where an 'inverse temporal cascade' is important for the shift of variance from high to low frequencies. Any mechanism, involving eddies or not, leading to such a cascade thus requires a source of spectral energy at high frequencies which can be provided by the eddies. It is beyond the scope of this study to analyze the exact mechanisms at play in ~~the HIGH simulation~~HR-CESM, but
450 it will be the subject of further study.

Naturally, the comparison between observations and model results is fraught with challenges, not least of which is the choice of an appropriate detrending procedure. The inadequate removal of the forced signal in the observations leads to biased regression patterns (Brown et al., 2015). In the model simulations the forcing is held constant and there is only a modest model drift to detrend (Fig. 1) for which we chose to a second order polynomial. The observations are based on the climate
455 system's response to non-stationary forcing and we chose the scaled multi-model mean approach (Frankcombe et al., 2015). Here the detrending signal is derived from the multi-model mean of the CMIP5 models which are biased in their own ways and have different relative climate sensitivities to different forcings. ~~Furthermore~~Also, the external forcing prescribed in the CMIP5 models is in itself uncertain and hence may alter the relative contribution due to external forcing and internal variability. Furthermore, the atmospheric grid spacing ~~decreases from 1° in the LOW to 0.5° in the HIGH simulation~~is refined from 1°in
460 LR-CESM to 0.5°in HR-CESM. However, no new essential atmospheric processes are resolved, so no significant changes are expected apart from coupling to different ocean boundary conditions.

These caveats do not detract from our main point which is to emphasize that low frequency variability may be underestimated in climate models with low-resolution ocean model components and that representing mesoscale eddies in climate models can improve the simulation of this variability. Of course, we showed this here only for the CESM but expect the
465 improvement of multidecadal variability to be generalizable to other coupled climate models, as some of the features like enhanced vertical heat transport are consistent with results obtained with other models (Griffies et al., 2015). The introduction of high frequency variability through mesoscale ocean features and the reduced ocean state bias can further improve the simulations' multidecadal variability skill. Certainly, better eddy parametrizations may improve shortcomings of the traditional Gent-McWilliams approach (Zanna et al., 2017). ~~A recent study~~ Recently, Mann et al. (2020) claimed an absence of
470 evidence for multidecadal ~~variability~~oscillations in CMIP5 models~~(Mann et al., 2020),~~, defined as spectral peaks above a null hypothesis, but all these models use non-eddying ocean components. As most CMIP6 models outside the High Resolution Model Intercomparison Project ~~(Haarsma et al., 2016)~~(HiResMIP, Haarsma et al. (2016)) still use non-eddying ocean com-

ponents, not much improvement is expected on the representation of ~~multidecacal~~ multidecadal variability in these models compared to CMIP5 models.

475 Internal variability obscures any forced GMST signal and periods of accelerated and decelerated warming are observed, such as the recent warming trend slowdown (Medhaug et al., 2017). Many studies use global circulation models with coarse resolution ocean components to investigate, for example, the origin of these so-called hiatuses (e.g. Maher et al. (2014)). In light of our findings, estimates of the frequency and magnitude of excursions from the forced trend may be systematically low biased in low-resolution models, as internal multidecadal variability is underestimated. The increased internal variability

480 also implies that the attribution of forced signals becomes more difficult and the issue of the origin of the recent warming trend slowdown may therefore never be satisfactorily resolved (Hedemann et al., 2017). Finally, our finding of stronger than previously modelled multidecadal OHC variability underlines the necessity of continued, long-term observations of the ~~ocean heat content~~ oceans with the ARGO program.

Code and data availability. The analysis scripts are available at `zenodo link to final code repository`, while the model out-

485 put is stored at SURFsara and available upon request to the corresponding author.

Author contributions. AJ, AvdH, and HD conceived the presented ideas in this study. AJ performed the analysis and wrote the manuscript. AvdH and HD contributed to writing the paper.

Competing interests. The authors declare that they have no conflict of interest.

Acknowledgements. This work was carried out under the program of the Netherlands Earth System Science Centre (NESSC), financially

490 supported by the Ministry of Education, Culture and Science (OCW) (Grantnr. 024.002.001). The computations were performed on the Cartesius high performance computer at SURFsara in Amsterdam. Use of the Cartesius computing facilities was sponsored by the Netherlands Science Foundation (NWO) under the project 15502. We thank Michael Kliphuis (IMAU) for carrying out the computations.

References

Berloff, P., McC. Hogg, A., and Dewar, W.: The turbulent oscillator: A mechanism of low-frequency variability of the wind-driven gyres, Journal of Physical Oceanography, 37, 2363–2386, https://doi.org/10.1175/JPO3118.1, 2007a.

Berloff, P. S., Dewar, W., Kravtsov, S., and McWilliams, J. C.: Ocean Eddy Dynamics in a Coupled Ocean–Atmosphere Model*, Journal of Physical Oceanography, 37, 1103–1121, https://doi.org/10.1175/JPO3041.1, 2007b.

Biastoch, A., Lutjeharms, J. R. E., Böning, C. W., and Scheinert, M.: Mesoscale perturbations control inter-ocean exchange south of Africa, Geophysical Research Letters, 35, L20 602, https://doi.org/10.1029/2008GL035132, 2008.

Bindoff, N. L., Stott, P. A., Stott, Mirle, K., Uk, M. R. A., Canada, N. G., Gutzler, D., Republic, S.-k. M., Uk, D. M., Germany, T. M., Uk, D. P., and France, A. R.: Detection and Attribution of Climate Change: from Global to Regional, in: Climate Change 2013 - The Physical Science Basis, edited by Intergovernmental Panel on Climate Change, vol. 9781107057, pp. 867–952, Cambridge University Press, Cambridge, https://doi.org/10.1017/CBO9781107415324.022, 2013.

Brown, P. T., Li, W., and Xie, S.-P.: Regions of significant influence on unforced global mean surface air temperature variability in climate models, Journal of Geophysical Research: Atmospheres, 120, 480–494, https://doi.org/10.1002/2014JD022576, 2015.

Buckley, M. W. and Marshall, J.: Observations, inferences, and mechanisms of the Atlantic Meridional Overturning Circulation: A review, Reviews of Geophysics, 54, 5–63, https://doi.org/10.1002/2015RG000493, 2016.

Cai, W., Wu, L., Lengaigne, M., Li, T., McGregor, S., Kug, J. S., Yu, J. Y., Stuecker, M. F., Santoso, A., Li, X., Ham, Y. G., Chikamoto, Y., Ng, B., McPhaden, M. J., Du, Y., Dommenget, D., Jia, F., Kajtar, J. B., Keenlyside, N., Lin, X., Luo, J. J., Martín-Rey, M., Ruprich-Robert, Y., Wang, G., Xie, S. P., Yang, Y., Kang, S. M., Choi, J. Y., Gan, B., Kim, G. I., Kim, C. E., Kim, S., Kim, J. H., and Chang, P.: Pantropical climate interactions, Science, 363, https://doi.org/10.1126/science.aav4236, 2019.

Cheung, A. H., Mann, M. E., Steinman, B. A., Frankcombe, L. M., England, M. H., and Miller, S. K.: Comparison of Low-Frequency Internal Climate Variability in CMIP5 Models and Observations, Journal of Climate, 30, 4763–4776, https://doi.org/10.1175/JCLI-D-16-0712.1, 2017.

Chylek, P., Folland, C. K., Dijkstra, H. A., Lesins, G., and Dubey, M. K.: Ice-core data evidence for a prominent near 20 year time-scale of the Atlantic Multidecadal Oscillation, Geophysical Research Letters, 38, n/a–n/a, https://doi.org/10.1029/2011GL047501, 2011.

Couvelard, X., Dumas, F., Garnier, V., Ponte, A. L., Talandier, C., and Treguier, A. M.: Mixed layer formation and restratification in presence of mesoscale and submesoscale turbulence, Ocean Modelling, 96, 243–253, https://doi.org/10.1016/j.ocemod.2015.10.004, 2015.

D'Arrigo, R., Villalba, R., and Wiles, G.: Tree-ring estimates of Pacific decadal climate variability, Climate Dynamics, 18, 219–224, https://doi.org/10.1007/s003820100177, 2001.

Dee, S., Parsons, L., Loope, G., Overpeck, J., Ault, T., and Emile-Geay, J.: Improved spectral comparisons of paleoclimate models and observations via proxy system modeling: Implications for multi-decadal variability, Earth and Planetary Science Letters, 476, 34–46, https://doi.org/10.1016/j.epsl.2017.07.036, 2017.

Delworth, T., Manabe, S., and Stouffer, R. J.: Interdecadal variations of the thermohaline circulation in a coupled ocean-atmosphere model, https://doi.org/10.1175/1520-0442(1993)006<1993:IVOTTC>2.0.CO;2, 1993.

Delworth, T. L. and Mann, M. E.: Observed and simulated multidecadal variability in the Northern Hemisphere, Climate Dynamics, 16, 661–676, https://doi.org/10.1007/s003820000075, 2000.

Delworth, T. L., Rosati, A., Anderson, W., Adcroft, A. J., Balaji, V., Benson, R., Dixon, K., Griffies, S. M., Lee, H.-C., Pacanowski, R. C., Vecchi, G. A., Wittenberg, A. T., Zeng, F., and Zhang, R.: Simulated Climate and Climate Change in the GFDL CM2.5 High-Resolution Coupled Climate Model, Journal of Climate, 25, 2755–2781, https://doi.org/10.1175/JCLI-D-11-00316.1, 2012.

Delworth, T. L., Zeng, F., Rosati, A., Vecchi, G. A., and Wittenberg, A. T.: A Link between the Hiatus in Global Warming and North American Drought, Journal of Climate, 28, 3834–3845, https://doi.org/10.1175/JCLI-D-14-00616.1, 2015.

Deser, C., Alexander, M. a., Xie, S.-P., and Phillips, A. S.: Sea Surface Temperature Variability: Patterns and Mechanisms, vol. 2, https://doi.org/10.1146/annurev-marine-120408-151453, 2010.

Deser, C., Lehner, F., Rodgers, K. B., Ault, T., Delworth, T. L., DiNezio, P. N., Fiore, A., Frankignoul, C., Fyfe, J. C., Horton, D. E., Kay, J. E., Knutti, R., Lovenduski, N. S., Marotzke, J., McKinnon, K. A., Minobe, S., Randerson, J., Screen, J. A., Simpson, I. R., and Ting, M.: Insights from Earth system model initial-condition large ensembles and future prospects, Nature Climate Change, 10, 277–286, https://doi.org/10.1038/s41558-020-0731-2, 2020.

Dijkstra, H. A.: Nonlinear Climate Dynamics, Cambridge University Press, New York, USA, 2013.

Dijkstra, H. A.: A Normal Mode Perspective of Intrinsic Ocean-Climate Variability, Annual Review of Fluid Mechanics, 48, 341–363, https://doi.org/10.1146/annurev-fluid-122414-034506, 2016.

Dufour, C. O., Morrison, A. K., Griffies, S. M., Frenger, I., Zanowski, H., and Winton, M.: Preconditioning of the Weddell Sea polynya by the ocean mesoscale and dense water overflows, Journal of Climate, 30, 7719–7737, https://doi.org/10.1175/JCLI-D-16-0586.1, 2017.

Durbin, J. and Koopman, S. J.: Time Series Analysis by State Space Methods: Second Edition, Oxford Statistical Science Series, OUP Oxford, 2012.

Eden, C. and Jung, T.: North Atlantic Interdecadal Variability: Oceanic Response to the North Atlantic Oscillation (1865–1997), Journal of Climate, 14, 676–691, https://doi.org/10.1175/1520-0442(2001)014<0676:NAIVOR>2.0.CO;2, 2001.

England, M. H., McGregor, S., Spence, P., Meehl, G. a., Timmermann, A., Cai, W., Gupta, A. S., McPhaden, M. J., Purich, A., and Santoso, A.: Recent intensification of wind-driven circulation in the Pacific and the ongoing warming hiatus, Nature Climate Change, 4, 222–227, https://doi.org/10.1038/nclimate2106, 2014.

Felis, T., Suzuki, A., Kuhnert, H., Rimbu, N., and Kawahata, H.: Pacific Decadal Oscillation documented in a coral record of North Pacific winter temperature since 1873, Geophysical Research Letters, 37, n/a–n/a, https://doi.org/10.1029/2010GL043572, 2010.

Frajka-Williams, E., Beaulieu, C., and Duchez, A.: Emerging negative Atlantic Multidecadal Oscillation index in spite of warm subtropics, Scientific Reports, 7, 1–8, https://doi.org/10.1038/s41598-017-11046-x, 2017.

Frankcombe, L. M., Dijkstra, H. A., and von der Heydt, A.: Noise-Induced Multidecadal Variability in the North Atlantic: Excitation of Normal Modes, Journal of Physical Oceanography, 39, 220–233, https://doi.org/10.1175/2008JPO3951.1, 2009.

Frankcombe, L. M., England, M. H., Mann, M. E., and Steinman, B. A.: Separating internal variability from the externally forced climate response, Journal of Climate, 28, 8184–8202, https://doi.org/10.1175/JCLI-D-15-0069.1, 2015.

Frankcombe, L. M., England, M. H., Kajtar, J. B., Mann, M. E., and Steinman, B. A.: On the Choice of Ensemble Mean for Estimating the Forced Signal in the Presence of Internal Variability, Journal of Climate, 31, 5681–5693, https://doi.org/10.1175/JCLI-D-17-0662.1, 2018.

Gebbie, G. and Huybers, P.: The Little Ice Age and 20th-century deep Pacific cooling, Science, 363, 70–74, https://doi.org/10.1126/science.aar8413, 2019.

Gent, P. R. and McWilliams, J. C.: Isopycnal Mixing in Ocean Circulation Models, J. Phys. Oceanogr., 20, 150–155, https://doi.org/10.1175/1520-0485, 1990.

Ghil, M., Allen, M. R., Dettinger, M. D., Ide, K., Kondrashov, D., Mann, M. E., Robertson, A. W., Saunders, A., Tian, Y., Varadi, F., and Yiou, P.: Advanced spectral methods for climatic time series, Reviews of Geophysics, 40, https://doi.org/10.1029/2000RG000092, 2002.

Gray, S. T., Graumlich, L. J., Betancourt, J. L., and Pederson, G. T.: A tree-ring based reconstruction of the Atlantic Multidecadal Oscillation since 1567 A.D., Geophysical Research Letters, 31, n/a–n/a, https://doi.org/10.1029/2004GL019932, 2004.

570 Griffies, S. M., Winton, M., Anderson, W. G., Benson, R., Delworth, T. L., Dufour, C. O., Dunne, J. P., Goddard, P., Morrison, A. K., Rosati, A., Wittenberg, A. T., Yin, J., and Zhang, R.: Impacts on Ocean Heat from Transient Mesoscale Eddies in a Hierarchy of Climate Models, Journal of Climate, 28, 952–977, https://doi.org/10.1175/JCLI-D-14-00353.1, 2015.

Gulev, S. K., Latif, M., Keenlyside, N., Park, W., and Koltermann, K. P.: North Atlantic Ocean control on surface heat flux on multidecadal timescales, Nature, 499, 464–467, https://doi.org/10.1038/nature12268, 2013.

575 Haarsma, R. J., Roberts, M. J., Vidale, P. L., Catherine, A., Bellucci, A., Bao, Q., Chang, P., Corti, S., Fučkar, N. S., Guemas, V., Von Hardenberg, J., Hazeleger, W., Kodama, C., Koenigk, T., Leung, L. R., Lu, J., Luo, J. J., Mao, J., Mizielinski, M. S., Mizuta, R., Nobre, P., Satoh, M., Scoccimarro, E., Semmler, T., Small, J., and Von Storch, J. S.: High Resolution Model Intercomparison Project (HighResMIP v1.0) for CMIP6, Geoscientific Model Development, 9, 4185–4208, https://doi.org/10.5194/gmd-9-4185-2016, 2016.

Häkkinen, S., Rhines, P. B., and Worthen, D. L.: Heat content variability in the North Atlantic Ocean in ocean reanalyses, Geophysical 580 Research Letters, 42, 2901–2909, https://doi.org/10.1002/2015GL063299, 2015.

Hallberg, R.: Using a resolution function to regulate parameterizations of oceanic mesoscale eddy effects, Ocean Modelling, 72, 92–103, https://doi.org/10.1016/j.ocemod.2013.08.007, 2013.

Hallberg, R. and Gnanadesikan, A.: The Role of Eddies in Determining the Structure and Response of the Wind-Driven Southern Hemisphere Overturning: Results from the Modeling Eddies in the Southern Ocean (MESO) Project, Journal of Physical Oceanography, 36, 2232– 585 2252, https://doi.org/10.1175/JPO2980.1, 2006.

Hasselmann, K.: Stochastic climate models Part I. Theory, Tellus, 28, 473–485, https://doi.org/10.3402/tellusa.v28i6.11316, 1976.

Hedemann, C., Mauritsen, T., Jungclaus, J., and Marotzke, J.: The subtle origins of surface-warming hiatuses, Nature Climate Change, 7, 336–339, https://doi.org/10.1038/nclimate3274, 2017.

Hegerl, G. and Zwiers, F.: Use of models in detection and attribution of climate change, Wiley Interdisciplinary Reviews: Climate Change, 590 2, 570–591, https://doi.org/10.1002/wcc.121, 2011.

Henley, B. J., Gergis, J., Karoly, D. J., Power, S., Kennedy, J., and Folland, C. K.: A Tripole Index for the Interdecadal Pacific Oscillation, Climate Dynamics, 45, 3077–3090, https://doi.org/10.1007/s00382-015-2525-1, 2015.

Hogg, A. M. C. and Blundell, J. R.: Interdecadal Variability of the Southern Ocean, Journal of Physical Oceanography, 36, 1626–1645, https://doi.org/10.1175/JPO2934.1, 2006.

595 Huck, T., Arzel, O., and Sévellec, F.: Multidecadal Variability of the Overturning Circulation in Presence of Eddy Turbulence, Journal of Physical Oceanography, 45, 157–173, https://doi.org/10.1175/jpo-d-14-0114.1, 2014.

Hurrell, J. W., Holland, M. M., Gent, P. R., Ghan, S., Kay, J. E., Kushner, P. J., Lamarque, J.-F., Large, W. G., Lawrence, D., Lindsay, K., Lipscomb, W. H., Long, M. C., Mahowald, N., Marsh, D. R., Neale, R. B., Rasch, P., Vavrus, S., Vertenstein, M., Bader, D., Collins, W. D., Hack, J. J., Kiehl, J., and Marshall, S.: The Community Earth System Model: A Framework for Collaborative Research, Bulletin of the 600 American Meteorological Society, 94, 1339–1360, https://doi.org/10.1175/BAMS-D-12-00121.1, 2013.

Jüling, A., Viebahn, J. P., Drijfhout, S. S., and Dijkstra, H. A.: Energetics of the Southern Ocean Mode, Journal of Geophysical Research: Oceans, https://doi.org/10.1029/2018jc014191, 2018.

Kajtar, J. B., Collins, M., Frankcombe, L. M., England, M. H., Osborn, T. J., and Juniper, M.: Global mean surface temperature response to large-scale patterns of variability in observations and CMIP5, Geophysical Research Letters, https://doi.org/10.1029/2018GL081462, 2019.

Kay, J. E., Deser, C., Phillips, A., Mai, A., Hannay, C., Strand, G., Arblaster, J. M., Bates, S. C., Danabasoglu, G., Edwards, J., Holland, M., Kushner, P., Lamarque, J. F., Lawrence, D., Lindsay, K., Middleton, A., Munoz, E., Neale, R., Oleson, K., Polvani, L., and Vertenstein, M.: The community earth system model (CESM) large ensemble project : A community resource for studying climate change in the presence of internal climate variability, Bulletin of the American Meteorological Society, 96, 1333–1349, https://doi.org/10.1175/BAMS-D-13-00255.1, 2015.

Kerr, R. A.: A North Atlantic Climate Pacemaker for the Centuries, Science, 288, 1984–1985, 2000.

Kim, W. M., Yeager, S., Chang, P., and Danabasoglu, G.: Low-frequency North Atlantic climate variability in the community earth system model large ensemble, Journal of Climate, 31, 787–813, https://doi.org/10.1175/JCLI-D-17-0193.1, 2018.

Kirtman, B. P., Bitz, C., Bryan, F., Collins, W., Dennis, J., Hearn, N., Kinter, J. L., Loft, R., Rousset, C., Siqueira, L., Stan, C., Tomas, R., and Vertenstein, M.: Impact of ocean model resolution on CCSM climate simulations, Climate Dynamics, 39, 1303–1328, https://doi.org/10.1007/s00382-012-1500-3, 2012.

Knudsen, M. F., Seidenkrantz, M.-S., Jacobsen, B. H., and Kuijpers, A.: Tracking the Atlantic Multidecadal Oscillation through the last 8,000 years, Nature Communications, 2, 178, https://doi.org/10.1038/ncomms1186, 2011.

Kosaka, Y. and Xie, S.-P.: Recent global-warming hiatus tied to equatorial Pacific surface cooling., Nature, 501, 403–7, https://doi.org/10.1038/nature12534, 2013.

Kumar, A. and Wen, C.: An Oceanic Heat Content–Based Definition for the Pacific Decadal Oscillation, Monthly Weather Review, 144, 3977–3984, https://doi.org/10.1175/MWR-D-16-0080.1, https://journals.ametsoc.org/doi/10.1175/MWR-D-16-0080.1, 2016.

Kushnir, Y.: Interdecadal Variations in North Atlantic Sea Surface Temperature and Associated Atmospheric Conditions, Journal of Climate, 7, 141–157, https://doi.org/10.1175/1520-0442(1994)007<0141:IVINAS>2.0.CO;2, http://journals.ametsoc.org/doi/10.1175/1520-0442(1994)007{%}3C0141:IVINAS{%}3E2.0.CO;2, 1994.

Le Bars, D., Viebahn, J. P., and Dijkstra, H. A.: A Southern Ocean mode of multidecadal variability, Geophysical Research Letters, 43, 2102–2110, https://doi.org/10.1002/2016GL068177, 2016.

MacDonald, G. M.: Variations in the Pacific Decadal Oscillation over the past millennium, Geophysical Research Letters, 32, L08 703, https://doi.org/10.1029/2005GL022478, 2005.

Maher, N., Gupta, A. S., and England, M. H.: Drivers of decadal hiatus periods in the 20th and 21st centuries, Geophysical Research Letters, 41, 5978–5986, https://doi.org/10.1002/2014GL060527, 2014.

Maher, N., Milinski, S., Suarez-Gutierrez, L., Botzet, M., Dobrynin, M., Kornblueh, L., Kröger, J., Takano, Y., Ghosh, R., Hedemann, C., Li, C., Li, H., Manzini, E., Notz, D., Putrasahan, D., Boysen, L., Claussen, M., Ilyina, T., Olonscheck, D., Raddatz, T., Stevens, B., and Marotzke, J.: The Max Planck Institute Grand Ensemble: Enabling the Exploration of Climate System Variability, Journal of Advances in Modeling Earth Systems, 11, 2050–2069, https://doi.org/10.1029/2019MS001639, 2019.

Mann, M. E., Steinman, B. A., and Miller, S. K.: Absence of internal multidecadal and interdecadal oscillations in climate model simulations, Nature Communications, 11, 49, https://doi.org/10.1038/s41467-019-13823-w, 2020.

Mantua, N. J., Hare, S. R., Zhang, Y., Wallace, J. M., and Francis, R. C.: A Pacific Interdecadal Climate Oscillation with Impacts on Salmon Production, Bulletin of the American Meteorological Society, 78, 1069–1079, https://doi.org/10.1175/1520-0477(1997)078<1069:APICOW>2.0.CO;2, 1997.

Manucharyan, G. E., Thompson, A. F., and Spall, M. A.: Eddy Memory Mode of Multidecadal Variability in Residual-Mean Ocean Circulations with Application to the Beaufort Gyre, Journal of Physical Oceanography, 47, 855–866, https://doi.org/10.1175/JPO-D-16-0194.1, 2017.

Martin, P. E., Arbic, B. K., McC. Hogg, A., Kiss, A. E., Munroe, J. R., and Blundell, J. R.: Frequency-domain Analysis of the Energy Budget in an Idealized, Coupled, Ocean-Atmosphere Model, Journal of Climate, pp. 707–726, https://doi.org/10.1175/jcli-d-19-0118.1, 2019.

McCabe, G. J. and Palecki, M. A.: Multidecadal climate variability of global lands and oceans, International Journal of Climatology, 26, 849–865, https://doi.org/10.1002/joc.1289, 2006.

McWilliams, J. C.: The nature and consequences of oceanic eddies, in: Eddy-Resolving Ocean Modeling, vol. 1, pp. 5–15, Cambridge University Press, https://doi.org/10.1029/177GM03, 2008.

Medhaug, I., Stolpe, M. B., Fischer, E. M., and Knutti, R.: Reconciling controversies about the 'global warming hiatus', Nature, 545, 41–47, https://doi.org/10.1038/nature22315, 2017.

Newman, M., Alexander, M. A., Ault, T. R., Cobb, K. M., Deser, C., Di Lorenzo, E., Mantua, N. J., Miller, A. J., Minobe, S., Nakamura, H., Schneider, N., Vimont, D. J., Phillips, A. S., Scott, J. D., and Smith, C. A.: The Pacific decadal oscillation, revisited, Journal of Climate, 29, 4399–4427, https://doi.org/10.1175/JCLI-D-15-0508.1, 2016.

O'Mara, N. A., Cheung, A. H., Kelly, C. S., Sandwick, S., Herbert, T. D., Russell, J. M., Abella-Gutiérrez, J., Dee, S. G., Swarzenski, P. W., and Herguera, J. C.: Subtropical Pacific Ocean Temperature Fluctuations in the Common Era: Multidecadal Variability and Its Relationship With Southwestern North American Megadroughts, Geophysical Research Letters, 46, 14 662–14 673, https://doi.org/10.1029/2019GL084828, 2019.

Park, S., Deser, C., and Alexander, M. A.: Estimation of the Surface Heat Flux Response to Sea Surface Temperature Anomalies over the Global Oceans, Journal of Climate, 18, 4582–4599, https://doi.org/10.1175/JCLI3521.1, http://journals.ametsoc.org/doi/10.1175/JCLI3521.1, 2005.

Parsons, L. A., Loope, G. R., Overpeck, J. T., Ault, T. R., Stouffer, R., and Cole, J. E.: Temperature and Precipitation Variance in CMIP5 Simulations and Paleoclimate Records of the Last Millennium, Journal of Climate, 30, 8885–8912, https://doi.org/10.1175/JCLI-D-16-0863.1, 2017.

Penduff, T., Juza, M., Barnier, B., Zika, J., Dewar, W. K., Treguier, A.-M. M., Molines, J.-M. M., and Audiffren, N.: Sea Level Expression of Intrinsic and Forced Ocean Variabilities at Interannual Time Scales, Journal of Climate, 24, 5652–5670, https://doi.org/10.1175/JCLI-D-11-00077.1, 2011.

Penduff, T., Barnier, B., Terray, L., Bessières, L., Sérazin, G., S.Gregorio, Brankart, J.-M., Moine, M.-P., Molines, J.-M., and P.Brasseur: Ensembles of eddying ocean simulations for climate, CLIVAR Exchanges No. 65, 19, 26–29, 2014.

Politis, D. N. and Romano, J. P.: The Stationary Bootstrap, Journal of the American Statistical Association, 89, 1303–1313, https://doi.org/10.1080/01621459.1994.10476870, https://www.tandfonline.com/doi/full/10.1080/01621459.1994.10476870, 1994.

Power, S., Casey, T., Folland, C., Colman, A., and Mehta, V.: Inter-decadal modulation of the impact of ENSO on Australia, Climate Dynamics, 15, 319–324, https://doi.org/10.1007/s003820050284, 1999.

Rayner, N. A., Parker, D. E., Horton, E. B., Folland, C. K., Alexander, L. V., and Rowell, D. P.: Global analyses of sea surface temperature, sea ice, and night marine air temperature since the late nineteenth century, Journal of Geophysical Research, 108, 4407, https://doi.org/10.1029/2002JD002670, 2003.

Roberts, C. D., Palmer, M. D., Allan, R. P., Desbruyeres, D., Hyder, P., Liu, C., and Smith, D.: Surface flux and ocean heat transport convergence contributions to seasonal and interannual variations of ocean heat content, Journal of Geophysical Research: Oceans, 122, 726–744, https://doi.org/10.1002/2016JC012278, http://doi.wiley.com/10.1002/2016JC012278, 2017.

680 Ruprich-Robert, Y., Delworth, T., Msadek, R., Castruccio, F., Yeager, S., and Danabasoglu, G.: Impacts of the Atlantic Multidecadal Variability on North American Summer Climate and Heat Waves, Journal of Climate, 31, 3679–3700, https://doi.org/10.1175/JCLI-D-17-0270.1, 2018.

Simpkins, G. R., Ciasto, L. M., and England, M. H.: Observed variations in multidecadal Antarctic sea ice trends during 1979-2012, Geophysical Research Letters, 40, 3643–3648, https://doi.org/10.1002/grl.50715, 2013.

685 Small, R. J., Bacmeister, J., Bailey, D., Baker, A., Bishop, S., Bryan, F., Caron, J., Dennis, J., Gent, P., Hsu, H., Jochum, M., Lawrence, D., Muñoz, E., DiNezio, P., Scheitlin, T., Tomas, R., Tribbia, J., Tseng, Y., and Vertenstein, M.: A new synoptic scale resolving global climate simulation using the Community Earth System Model, Journal of Advances in Modeling Earth Systems, 6, 1065–1094, https://doi.org/10.1002/2014MS000363, 2014.

Small, R. J., Bryan, F. O., Bishop, S. P., Larson, S., and Tomas, R. A.: What Drives Upper-Ocean Temperature Variability in Coupled Climate
690 Models and Observations?, Journal of Climate, 33, 577–596, https://doi.org/10.1175/JCLI-D-19-0295.1, http://journals.ametsoc.org/doi/10.1175/JCLI-D-19-0295.1, 2020.

Steinman, B. A., Mann, M. E., and Miller, S. K.: Atlantic and Pacific multidecadal oscillations and Northern Hemisphere temperatures, Science, 347, 988–991, https://doi.org/10.1126/science.1257856, 2015.

Stocker, T. F., Qin, D., Plattner, G.-K., Tignor, M., Allen, S. K., Boschung, J., Nauels, A., Xia, Y., And, V. B., and P.M. Midgley (eds.):
695 IPCC, 2013: Climate Change 2013: The Physical Science Basis. Contribution of Working Group I to the Fifth Assessment Report of the Intergovernmental Panel on Climate Change, Cambridge University Press, Cambridge, https://doi.org/10.1017/CBO9781107415324, http://ebooks.cambridge.org/ref/id/CBO9781107415324, 2013.

Stolpe, M. B., Medhaug, I., and Knutti, R.: Contribution of Atlantic and Pacific Multidecadal Variability to Twentieth-Century Temperature Changes, Journal of Climate, 30, 6279–6295, https://doi.org/10.1175/JCLI-D-16-0803.1, 2017.

700 Sutton, R. T. and Hodson, D. L.: Ocean science: Atlantic Ocean forcing of North American and European summer climate, Science, 309, 115–118, https://doi.org/10.1126/science.1109496, 2005.

Taylor, K. E., Stouffer, R. J., and Meehl, G. A.: An overview of CMIP5 and the experiment design, Bulletin of the American Meteorological Society, 93, 485–498, https://doi.org/10.1175/BAMS-D-11-00094.1, 2012.

Te Raa, L. A. and Dijkstra, H. A.: Instability of the thermohaline ocean circulation on interdecadal timescales, Journal of Physical Oceanog-
705 raphy, 32, 138–160, https://doi.org/10.1175/1520-0485(2002)032<0138:IOTTOC>2.0.CO;2, 2002.

Trenberth, K. E.: Some Effects of Finite Sample Size and Persistence on Meteorological Statistics. Part I: Autocorrelations, Monthly Weather Review, 112, 2359–2368, https://doi.org/10.1175/1520-0493(1984)112<2359:SEOFSS>2.0.CO;2, 1984.

Trenberth, K. E. and Shea, D. J.: Atlantic hurricanes and natural variability in 2005, Geophysical Research Letters, 33, 1–4, https://doi.org/10.1029/2006GL026894, 2006.

710 Tulloch, R., Marshall, J., Hill, C., and Smith, K. S.: Scales, Growth Rates, and Spectral Fluxes of Baroclinic Instability in the Ocean, Journal of Physical Oceanography, 41, 1057–1076, https://doi.org/10.1175/2011JPO4404.1, 2011.

van Westen, R. M. and Dijkstra, H. A.: Southern Ocean Origin of Multidecadal Variability in the North Brazil Current, Geophysical Research Letters, 44, 10,510–540,548, https://doi.org/10.1002/2017GL074815, http://dx.doi.org/10.1002/2017GL074815, 2017.

Viebahn, J. P., Crommelin, D., and Dijkstra, H. A.: Towards a turbulence closure based on energy modes, Journal of Physical Oceanography, https://doi.org/10.1175/jpo-d-18-0117.1, 2018.

Wang, J., Yang, B., Ljungqvist, F. C., Luterbacher, J., Osborn, T. J., Briffa, K. R., and Zorita, E.: Internal and external forcing of multidecadal Atlantic climate variability over the past 1,200 years, Nature Geoscience, 10, 512–517, https://doi.org/10.1038/ngeo2962, 2017.

Weijer, W. and van Sebille, E.: Impact of Agulhas leakage on the Atlantic overturning circulation in the CCSM4, Journal of Climate, 27, 101–110, https://doi.org/10.1175/JCLI-D-12-00714.1, 2014.

Wieners, C. E., Dijkstra, H. A., and de Ruijter, W. P. M.: The interaction between the Western Indian Ocean and ENSO in CESM, Climate Dynamics, 52, 5153–5172, https://doi.org/10.1007/s00382-018-4438-2, 2019.

Zanna, L., Porta Mana, P., Anstey, J., David, T., and Bolton, T.: Scale-aware deterministic and stochastic parametrizations of eddy-mean flow interaction, Ocean Modelling, 111, 66–80, https://doi.org/10.1016/j.ocemod.2017.01.004, 2017.

Zanna, L., Khatiwala, S., Gregory, J. M., Ison, J., and Heimbach, P.: Global reconstruction of historical ocean heat storage and transport, Proceedings of the National Academy of Sciences, p. 201808838, https://doi.org/10.1073/pnas.1808838115, 2019.

Zhang, L. and Wang, C.: Multidecadal North Atlantic sea surface temperature and Atlantic meridional overturning circulation variability in CMIP5 historical simulations, Journal of Geophysical Research: Oceans, 118, 5772–5791, https://doi.org/10.1002/jgrc.20390, 2013.

Zhang, L., Delworth, T. L., Cooke, W., and Yang, X.: Natural variability of Southern Ocean convection as a driver of observed climate trends, Nature Climate Change, 9, 59–65, https://doi.org/10.1038/s41558-018-0350-3, https://doi.org/10.1038/s41558-018-0350-3, 2019a.

Zhang, R. and Delworth, T. L.: Impact of Atlantic multidecadal oscillations on India/Sahel rainfall and Atlantic hurricanes, Geophysical Research Letters, 33, L17 712, https://doi.org/10.1029/2006GL026267, 2006.

Zhang, R., Sutton, R., Danabasoglu, G., Kwon, Y., Marsh, R., Yeager, S. G., Amrhein, D. E., and Little, C. M.: A Review of the Role of the Atlantic Meridional Overturning Circulation in Atlantic Multidecadal Variability and Associated Climate Impacts, https://doi.org/10.1029/2019RG000644, https://onlinelibrary.wiley.com/doi/abs/10.1029/2019RG000644, 2019b.